



UNIVERSITY OF AMSTERDAM



MSc Physics and Astronomy
Track: Astronomy & Astrophysics

MASTER THESIS

Simulation of a proposed X-ray interferometry satellite

Using a scientific simulator
to realize the potential of X-ray interferometry

by

Erik J. Bootsma
12278858 (UVA)

August 20, 2024

60 ECTS

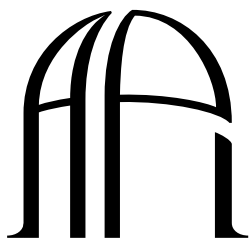
September 4, 2024 - August 20, 2024

Supervisors:

Dr. Phil Uttley (API)
Dr. Roland H. den Hartog (SRON)

Examiners

Dr. Phil Uttley (API)
Prof. dr. Ralph Wijers (API)



ANTON PANNEKOEK
INSTITUTE

SRON
Netherlands Institute for Space Research

Abstract

To resolve astrophysical sources, telescopes have reached the theoretical diffraction limit on angular resolution. A major exception being the X-ray bands, even though X-rays are very useful for probing astrophysical sources. This is due to the difficulty of manufacturing focusing optics for X-rays to sufficient precision. X-ray interferometry may hold the key to reach the theoretical diffraction limit in X-rays and resolve many scientifically interesting sources. An end-to-end simulator of the proposed spacecraft using X-ray interferometry is a very important tool. It can show scientists what is possible within mechanical limitations and inform engineers about the required tolerances. This thesis focuses on the corrections, improvements and expansions of the end-to-end simulator of the proposed space telescope. The simulator is sped up with an image reconstruction method, which is mostly independent of the number of photons. The effect of background is shown to be manageable. The reconstructed image is blurred, but retains the useful information in visible structures. The quality of the reconstructed images can be quantified and it was used to show the improvement that the number of source photons has on the reconstructed image quality.

Contents

1	Introduction	1
1.1	Context	1
1.2	Science cases	4
1.2.1	Cygnus X-1	4
1.2.2	AU Microscopii	5
1.3	X-ray interferometer	6
1.3.1	Willingale design	7
1.3.2	Fringe pattern	9
1.4	Simulator History	13
2	The Simulator	14
2.1	Images	17
2.1.1	Spectra	19
2.1.2	Background	19
2.2	Instrument	22
2.2.1	Main body	22
2.2.2	Baselines	22
2.2.3	Detector	26
2.3	Process	28
2.3.1	Energy sampling	28
2.3.2	Baseline selection	31
2.3.3	Pattern correction	31
2.4	Analysis	35
2.4.1	Image reconstruction	35
2.4.2	Periodogram	38
2.4.3	Image quality	41
3	Results	42
3.1	Speed comparison exact inverse Fourier transform and inverse fast Fourier transform	42
3.2	Background effects	45
3.3	Reconstructed image quality: number of photons	46
4	Discussion	48

Contents

4.1	Sum of squared residuals accuracy	48
4.2	Future work	55
4.2.1	Input data	55
4.2.2	Background function	55
4.2.3	Cosmic rays	56
4.2.4	More realistic detector	56
4.2.5	Path length perturbation sources	57
4.2.6	Spacecraft wobble correction	57
4.2.7	More testing	57
4.2.8	User manual	57
5	Conclusion	59
A	Iridium reflectivity	60
B	Timing data tables	62
C	Reconstructed images, their respective residuals, and sum of squared residuals values	64

List of Figures

1.1	Actual telescope resolution compared to theoretical limit.	3
1.2	Diagram of the X-ray interferometer optical bench.	8
1.3	Fresnel diffraction pattern.	12
2.1	Schematic overview of the structure of the end-to-end simulator.	15
2.2	Cygnus X-1 model image.	16
2.3	AU Microscopii model image.	18
2.4	Sagittarius A* model image.	19
2.5	Background sampling of the Cygnus X-1 model.	21
2.6	Spacecraft concept outline.	23
2.7	Silicon mirror reflectivity.	25
2.8	Effective area.	26
2.9	Detector quantum efficiency.	27
2.10	Sampled source spectrum.	29
2.11	Sampled source spectrum, with effective area included.	30
2.12	Sampled pure fringe pattern.	33
2.13	Sampled pure diffraction pattern.	34
2.14	Sampled full fringe and diffraction pattern.	34
2.15	Image reconstruction using the exact inverse Fourier transform and inverse fast Fourier transform methods.	38
2.16	Periodograms of Cygnus X-1.	39
2.17	More realistic periodogram of Cygnus X-1.	40
3.1	Timing of the exact inverse Fourier transform and the inverse fast Fourier transform.	44
3.2	The effect of background on image reconstruction.	46
3.3	The sum of squared residuals as a function of the number of source photons.	47
4.1	Residual without normalisation.	50
4.2	Residual with normalisation based on normalizing the means.	51
4.3	Residual with normalisation based on normalizing the sums.	52
4.4	Residual with normalisation based on the minimum and maximum pixel values.	53
4.5	Residual with normalisation using Equation 2.16.	54

A.1	Iridium reflectivity.	61
C.1	Reconstructed image and residual for 10^3 photons 1.	65
C.2	Reconstructed image and residual for 10^3 photons 2.	65
C.3	Reconstructed image and residual for 10^3 photons 3.	66
C.4	Reconstructed image and residual for 10^4 photons 1.	66
C.5	Reconstructed image and residual for 10^4 photons 2.	67
C.6	Reconstructed image and residual for 10^4 photons 3.	67
C.7	Reconstructed image and residual for 10^5 photons 1.	68
C.8	Reconstructed image and residual for 10^5 photons 2.	68
C.9	Reconstructed image and residual for 10^5 photons 3.	69
C.10	Reconstructed image and residual for 10^6 photons 1.	69
C.11	Reconstructed image and residual for 10^6 photons 2.	70
C.12	Reconstructed image and residual for 10^6 photons 3.	70
C.13	Reconstructed image and residual for 10^7 photons 1.	71
C.14	Reconstructed image and residual for 10^7 photons 2.	71
C.15	Reconstructed image and residual for 10^7 photons 3.	72

List of Tables

B.1	Timing data table of Figure 3.1 for the Cygnus X-1 input model.	63
B.2	Timing data table of Figure 3.1 for the AU Microscopii input model.	63
B.3	Timing data table of Figure 3.1 for the Sagittarius A* input model.	63
C.1	Sum of squared residuals values table of Figure 3.3.	64

List of Abbreviations

AOCS	attitude and orbit control system
AU Mic	AU Microscopii
BH	black hole
cdf	cumulative density function
Cyg X-1	Cygnus X-1
EHT	Event Horizon Telescope
eIFT	exact inverse Fourier transform
FoV	field of view
HMXB	high mass X-ray binary
IFFT	inverse fast Fourier transform
LETG	Low Energy Transmission Grating
pdf	probability density function
RMS	root-mean-square
Sgr A*	Sagittarius A*
SNR	signal to noise ratio
SSR	sum of squared residuals
TOA	time of arrival
XRI	X-ray interferometer

Chapter 1

Introduction

1.1 Context

X-rays are highly energetic photons with typical energies ranging between 100 eV and 100 keV and wavelengths ranging between 0.01 nm and 10 nm. In astronomy, X-rays are very useful for probing multiple different systems and physics. This is due to the fact that X-rays can be produced in significant amounts by both thermal and non-thermal processes. These include, but are not necessarily limited to, synchrotron radiation, Compton scattering, black body radiation, bremsstrahlung and line emission. The first two processes can in most cases be described using classical electrodynamics, while the last two processes are intrinsically quantum processes ([Blumenthal & Tucker 1974](#)). Black body radiation is always a thermal emission process. Compton scattering and bremsstrahlung can be produced by thermal and non-thermal processes. Researching X-rays from astronomical sources therefore allows for the probing of different physical systems, mechanisms and properties. Telescopes have, in most wavelength bands, reached the theoretical diffraction limit on angular resolution. The Rayleigh diffraction limit is given by

$$\theta_R \approx 1.22 \frac{\lambda}{d_{\text{telescope}}}, \quad (1.1)$$

with the angular resolution θ_R of a telescope with a diameter $d_{\text{telescope}}$, which images light at a wavelength λ . The X-ray bands are a major exception to telescopes reaching the Rayleigh diffraction limit ([Uttley et al. 2020](#)), see Figure 1.1. The radio telescopes probe much longer wavelengths and have bigger diameters, compared to X-ray telescopes. The effective telescope diameter increases significantly for radio interferometry telescopes, becoming nearly a full Earth-diameter for the Event Horizon Telescope (EHT) collaboration ([Collaboration et al. 2019](#)). The smaller wavelengths of X-rays are counteracted by the smaller telescope diameters, resulting in similar diffraction limits for radio and X-ray telescopes. Radio telescopes are able to get very

close to the diffraction limit, whereas X-ray telescopes are far from it. This is due to the difficulty of manufacturing focusing optics for X-rays to a precision of a fraction of the wavelength. A Wolter telescope, type I, II or III, is a mirror combination that focuses X-rays with two grazing incidence reflectors. These mirrors are paraboloid, and Hyperboloid or Ellipsoid in shape ([Wolter 1952a](#); [Wolter 1952b](#)). These curved mirrors cannot yet be shaped to the required precision to reach the theoretical angular resolution limit.

X-ray interferometry may hold the key to overcoming the challenges and achieving angular resolutions closer to the theoretical limit. The first detection of X-ray interference fringes were reported by [Cash et al. \(2000\)](#). This was followed by NASA-sponsored studies into the possibility of X-ray-interferometric telescopes in space ([Cash 2003](#); [Gendreau et al. 2003](#); [Cash et al. 2004](#); [Gendreau et al. 2009](#)). One of the major problems was that the proposed ideas required highly accurate formations of free flying spacecraft, which are up to 3×10^5 km apart ([Gendreau et al. 2004](#)). This was not yet feasible at the time. Then came the telephoto design by [Willingale \(2004\)](#) of an X-ray interferometer (XRI), resulting in an orders of magnitude more compact design, which made an XRI feasible within a single spacecraft. This spacecraft can achieve an expected resolution of $100 \mu\text{as}$ at 10\AA ($\sim 1.2 \text{ keV}$). This concept is still in the very early stages of development, and its simulation is the subject of this thesis.

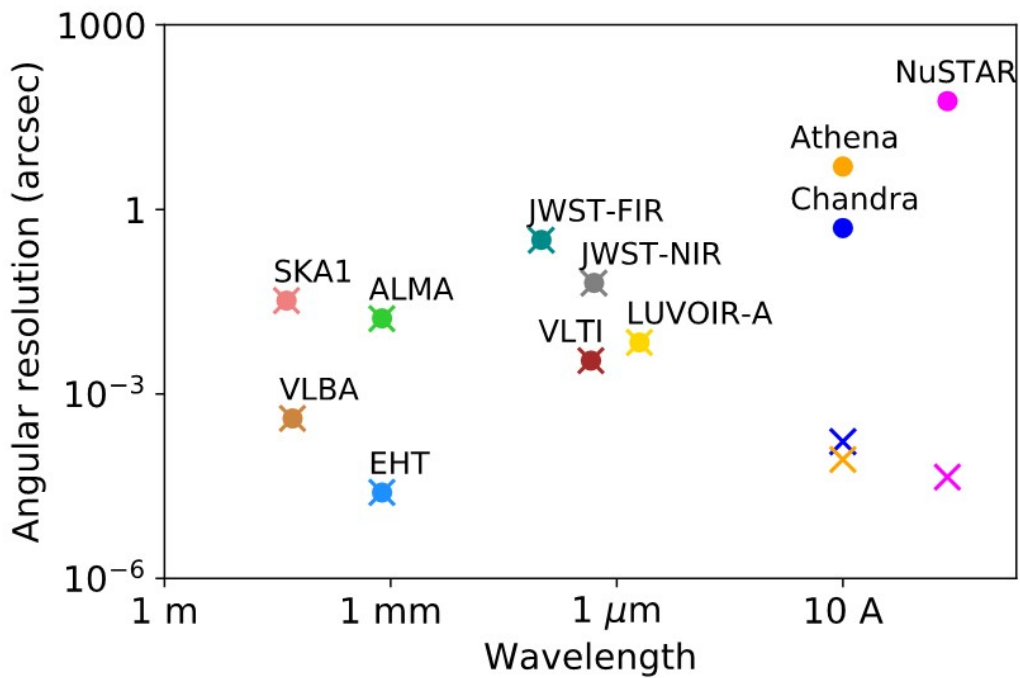


FIG. 1.1 – Comparison of actual angular resolution (circles) with the theoretical diffraction limit (crosses) for existing and foreseen telescopes from radio to X-rays. Only X-ray telescopes remain far from the theoretical limit. Adopted from Uttley et al. (2020).

1.2 Science cases

X-ray emission is strongly affected by the local conditions in astronomical objects, such as density and temperature, and offers a powerful probe, especially of regions of high temperature and density. Observing these objects in the X-ray bands thereby results in better understanding of conditions in the objects. These conditions can be tested against predictions of fundamental physics and how these result in the object itself, thereby also resulting in a better understanding of the observed object. Additionally, an XRI has the ability to image and take a spectrum simultaneously. Collecting more scientifically valuable data at once while "images have more power to inspire and change the direction of people's lives than any other tool at an astronomer's disposal" ([Uttley et al. 2021](#)). The following two objects are a subset of, and have been based on science cases proposed by [Uttley et al. \(2021\)](#). These objects are expected to be spatially resolvable using a single spacecraft XRI ([Uttley et al. 2020; Uttley et al. 2021](#)).

1.2.1 Cygnus X-1

The X-ray signature of Cygnus X-1 (Cyg X-1) was first discovered by [Bowyer et al. \(1965\)](#), there given the name Cyg X-1. In [1971](#) the variable nature of the source was first analysed by [Oda et al. \(1971\)](#), finding some periodicity. [Webster & Murdin \(1972\)](#) used spectrograms to measure HD 226868, also named HDE 226868, to calculate its variable radial velocity and thereby conclude that it is part of a binary system. Shortly thereafter, also using spectral data, [Bolton \(1972\)](#) showed that HDE 226868 and Cyg X-1 are part of the same system. Both [Webster & Murdin \(1972\)](#) and [Bolton \(1972\)](#) speculated that that the binary system contains a black hole (BH), the system was labeled a BH candidate by [Oda \(1977\)](#). After the works of [Reid et al. \(2011\)](#), [Orosz et al. \(2011\)](#), [Gou et al. \(2011\)](#) and others, the existence of a BH in the X-ray binary of Cyg X-1 was confirmed beyond reasonable doubt. Cyg X-1 is one of the most well-studied BH systems with multi wavelength data, spanning the radio, optical and X-ray wavebands.

Yet work by [Miller-Jones et al. \(2021\)](#) suggests a new BH mass of $21.2 \pm 2.2 M_{\odot}$, which is outside of the previous error margins. XRI can directly image the system, making it a visual binary ([Uttley et al. 2021](#)). This will allow for better measurements of the orbital velocities, as the orbits can be imaged and traced. This will in turn result in a more accurate BH mass, as fundamental system parameters can be directly measured from the images. The mass of the compact binary has implications for massive star winds. Massive star winds are, in turn, key ingredients for understanding massive stars and massive star binaries. They have the ability to significantly impact the evolutionary pathways of massive stars (which are the progenitors of explosive transients and gravitational wave sources). They additionally affect star formation in

solar nurseries and enrich their environment and increase the surrounding metallicity ([Kudritzki & Puls 2000](#)). High mass X-ray binaries (HMXBs) are expected to be a necessary step towards double degenerate systems, whose mergers are observed as gravitational wave events ([Giacobbo & Mapelli 2018](#)). In HMXBs, such as Cyg X-1, these winds drive changes in the accretion rate. Those changes affect the system's X-ray emission, which interacts with the wind material. This interaction can be used to study the properties of the wind itself when imaged by an XRI (see [Watanabe et al. 2006](#); [Grinberg et al. 2017](#); and [Martínez-Núñez et al. 2017](#)). Understanding the geometry of these winds will improve our binary evolution, X-ray binary and wind models. Direct imaging of the resolved winds, using an XRI, will allow for quantitative and qualitative measurements of the massive star wind properties (e.g. geometry).

Cyg X-1 shows jets ([Stirling et al. 2001](#)). Knowledge about the physics of jets, including the mechanisms that (re-)accelerate matter into and along the jet is limited due to many unknowns. Direct XRI imaging of the X-ray emitting regions of the jets and the accretion disk will allow for the study of jet evolution and the jet dependence on accretion properties. Simultaneous spectrographic data will further enhance understanding of the physics behind jets, disk winds and accretion as a whole. Additionally, wide-angle winds are also significant in the understanding of accretion processes. These winds have been detected in high-resolution spectra of Galactic BHs and it has been suggested that they can carry away enough mass and energy to quench radio jets ([Ponti et al. 2012](#)). Additionally, they have the potential to significantly destabilize the accretion disks that launch them ([Shields et al. 1986](#); [Muñoz-Darias et al. 2016](#)). Direct resolved imaging of disk winds will allow for the testing and improving of wind models. There is a potential for constraining the geometry of the wind and disk atmospheres through emission and by identifying the position of cooler and warmer components of the wind, even in unfavourable systems (e.g. smaller or unfavourable line-of-sight systems, [Uttley et al. 2021](#)).

1.2.2 AU Microscopii

AU Microscopii (AU Mic) was first mentioned in the Henry Draper catalogue, where it was classified as a K2 spectral type star ([Cannon & Pickering 1918](#)). It has since been revised with the most recent spectral typing of M1 ([Klein et al. 2021](#)). AU Mic has also been found to harbor orbiting exoplanets. Currently, it has three confirmed and one candidate exoplanets ([Plavchan et al. 2020](#); [Martoli et al. 2021](#); [Wittrock et al. 2023](#); [Donati et al. 2023](#)). The one that was discovered first is AU Mic b, discovered by [Plavchan et al. \(2020\)](#). They used the transit event observation, where a dip in the observed light curve is the result of the exoplanet (partially) eclipsing the host star. The detection of exoplanets around a star like AU Mic is challenging due to manifestations of magnetic activity on the star, which effects the star's emission

(see [Van Eyken et al. 2012](#); [Donati et al. 2016](#); and [Plavchan et al. 2020](#)).

Many stars emit X-rays from their coronae, the hot (up to several million K) outermost atmosphere layer. The heating mechanism of these coronae is not fully understood yet. It is expected to be primarily driven by magnetic effects [Drake & Stelzer \(2022\)](#). The cooling mechanism is emission of metallic spectral lines in the X-ray wavelength band ([Güdel 2004](#)). Currently, the only star with a resolvable corona is the sun. An XRI can spatially resolve the corona of AU Mic and other stars of similar angular size ([Uttley et al. 2021](#)), thereby furthering the understanding of the heating mechanisms of stellar coronae.

The ability to resolve the atmosphere of AU Mic, and other stars of similar angular size, also enables the ability for exoplanet measurements through direct imaging. Additionally, the exoplanets that cross the stellar disk in the line of sight provide the opportunity to study their atmospheres in the X-ray bands. When stars are observed as point sources, any variation in emission over the stellar surface manifests itself as systematic errors in the measured exoplanet parameters ([Czesla et al. 2009](#)). Spatially resolving the star's atmosphere can disentangle localized stellar brightness changes in the corona from the effects of a transiting exoplanet ([Uttley et al. 2021](#)). An exoplanet's X-ray transit depth measurement can probe the extent and density of the outer planetary atmosphere ([Poppenhaeger et al. 2013](#)). This would also allow for multi wavelength spectra to be taken of exoplanet atmospheres, which would increase the accuracy and understanding of the atmosphere composition. Potentially, resolved-disk X-ray transits can remove trends in observations at other wavelengths (linked to stellar variability) through reconstructions of the stellar chromosphere and photosphere based on the coronal structure ([Uttley et al. 2021](#)), with uncertainties in stellar parameters and variability currently being one of the main limiting factors in studying exoplanets, especially their atmospheres.

1.3 X-ray interferometer

The core interferometry principle of the XRI is that of the Michelson interferometer and is shown in Figure 1.2. Panel *c* shows the basic geometry used to produce interference fringes from two beams. These beams sample the incident wavefronts coming from a distant X-ray source. A detector will be placed where the two beams fully overlap, this slice will henceforth be referenced as the detector plane. Let L be the distance required to combine the beams, defined as the distance along the x-axis between the beams first touching to fully overlapping. Let θ_b be the angle between the beams and λ be the central wavelength, with a bandwidth $\Delta\lambda$. Then the fringe spacing along the y-axis, Δy , is given by

$$\Delta y = \frac{\lambda}{\theta_b}, \quad (1.2)$$

using the small angle approximation of θ_b . Let both beams have an equal width of W (sometimes referred to as W_b for clarity) and again using the small angle approximation of θ_b , then

$$\theta_b = \frac{W}{L}, \quad (1.3)$$

and

$$N_f = \frac{W}{\Delta y}, \quad (1.4)$$

with N_f the number of fringes across the overlapping beams. When optimizing the value of W and investigating the requirements using Δy , it can be useful to rewrite the above equations as

$$\Delta y = \sqrt{\frac{\lambda L}{N_f}}, \quad (1.5)$$

and

$$W = \sqrt{\lambda L N_f}, \quad (1.6)$$

with the maximum feasible L and minimum statistically required N_f being the limiting factors.

1.3.1 Willingale design

The baseline of the interferometer is set by the separation along the y-axis of mirrors M1 and M3, the collector mirrors, see Figure 1.2 panel *b*. The optical bench design by Willingale (2004) uses four flat mirrors, adding two combiner mirrors M2 and M4 to the collecting mirrors. The flat mirrors result in no focusing of the beams and therefore do not decrease the illuminated detector area, thus requiring a relatively larger detector area. The angle between the mirrors and the beams must be grazing, $\lesssim 2^\circ$, for X-ray photons to reflect in significant numbers. Let θ_g be the angle with respect to the x-axis at which the mirrors M1 and M3 are set, then M2 and M4 must be set at an angle $\theta_g - \frac{\theta_b}{4}$ for the beams to fully overlap. This set up results in the effective focal length F to be much greater than the distance L (Willingale 2004). Let the effective focal length be the distance, along the x-axis, from the fully overlapping beams, to a beam separation of D , given a beam angle θ_b . Then the effective focal length can be calculated as

$$F = \frac{\Delta y D}{\lambda}. \quad (1.7)$$

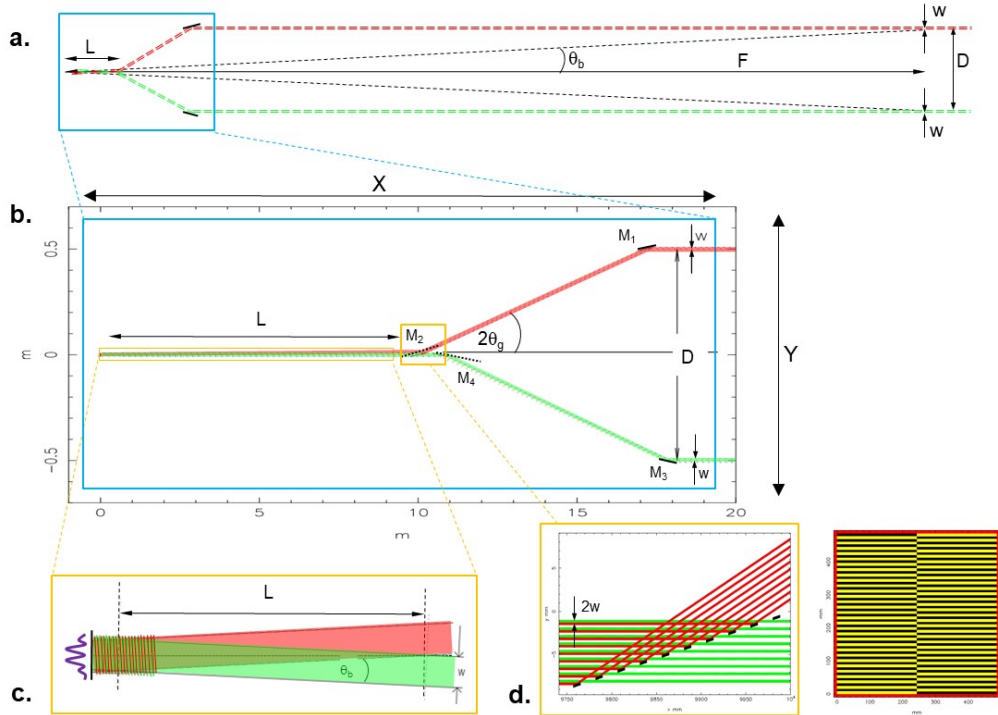


FIG. 1.2 – Summary of the single-spacecraft interferometer design ([Willingale 2004](#)). The interferometer’s combination of collector mirrors with axial combiner mirrors affords a long effective focal length F (see panel *a*) with compact interferometer dimensions (see panel *b* and note that vertical and horizontal dimensions are on different scales throughout). Collector mirrors M₁ and M₃ form the baseline D , directing parallel X-ray beams (of width W) through twice the grazing angle θ_g , to combiner mirrors M₂ and M₄. Mirror M₂ is slatted (panel *d*) to admit the beam from M₄, with slats/gaps of projected width w so that the offset angle θ_b causes a position-dependent optical path difference on the detector, enabling fringes to form (panel *c*). By alternating the slat pattern on the vertical halves of the mirror (right of panel *d*), fringes in the shadow of slats in one half of the mirror can be recovered in the gaps of the other half. Adopted from [Uttley et al. \(2020\)](#).

The fringe spacing Δy must be sufficiently large, such that current X-ray detectors are able to detect distinguishable fringes. Requiring the fringe spacing to be a factor three larger than the assumed a detector resolution of $\sim 10 \mu\text{m}$ (Willingale 2004), and taking a central wavelength $\lambda = 10 \text{ \AA}$, it follows from Equation 1.2 that $\theta_b \approx 6.9 \text{ as}$. Given the angles of the combining mirrors M2 and M4 and this small required θ_b , the mirrors must lie in approximately the same xz-plane as one another. Therefore this design requires M2 to be a slatted mirror, which acts as an X-ray beam combiner. An example is shown on panel *d* in Figure 1.2. The right Figure in this panel shows that the slatted mirror consists of two sets of slats and gaps that have been alternated halfway along the z-axis. This is to fill in the shadows cast by the slats and gaps in the beams. The projected slat/gap width w , as seen by the beam, sets the effective beam width. Thus $W = w$ holds for the interference physics. For the engineering aspect, the effective beam width W is set by the projected size, as seen by the beams, of the collecting mirrors M1 and M3. The discrepancy in the values of W and w may lead to stray X-rays, which can either be blocked or they will result in an increased background signal.

1.3.2 Fringe pattern

The total pattern in the y-plane at the x-position where the two beams fully overlap, is a multiplicative combination of the fringe pattern and the diffraction pattern. The fringes form due to the optical path length differences between photons from the two beams, provided that the optical path length difference ΔP is less than the longitudinal coherence length l_{coh} given by

$$l_{\text{coh}} = \frac{\lambda^2}{\Delta\lambda}. \quad (1.8)$$

The optical path length difference between the two interferometer arms is given by

$$\Delta P = -\Delta L \left(\frac{1}{\cos\left(\frac{\theta_b}{2}\right)} - 1 \right) + 2y \sin\left(\frac{\theta_b}{2}\right) + D \sin\theta, \quad (1.9)$$

with ΔL the distance along the x-axis between the combiner mirrors M2 and M4, y the y-position on the detector plane, and θ the off axis angle of the photon source (Willingale 2004). The off axis angle is defined as the projection of the two-dimensional angle by which the observed source is offset from the x-axis going through the centre of the XRI. The term $-\Delta L \left(\frac{1}{\cos\left(\frac{\theta_b}{2}\right)} - 1 \right)$ can be corrected for with the mirror alignment, to have the central fringe with $\theta = 0$ to be in the middle of the detector plane. This leaves

$$\Delta P = 2y \sin\left(\frac{\theta_b}{2}\right) + D \sin\theta. \quad (1.10)$$

The center of the fringe pattern has $\Delta P = 0$, rewriting the above equation gives

$$y_{\text{cent}} = -\frac{D \sin \theta}{2 \sin \left(\frac{\theta_b}{2}\right)}. \quad (1.11)$$

The fringe pattern has the shape

$$I_{\text{fringe}} \propto \cos^2 \left(\frac{\Delta\phi}{2} \right), \quad (1.12)$$

with I_{fringe} the intensity, due to the interference fringes, and $\Delta\phi$ the phase difference between the two beams given by

$$\Delta\phi = 2\pi \frac{\Delta P}{\lambda}. \quad (1.13)$$

Additionally, there is a diffraction pattern introduced by the slats in the slatted mirror M2. This pattern is independent of the fringe pattern and both patterns can thus be multiplied to get the total pattern. In Fourier space, this becomes a convolution, distorting the power spectrum. The diffraction can be described using the near field approximation of the Rayleigh-Sommerfeld integral (Fresnel diffraction), when

$$\frac{a^2 \theta_{\max}^2}{4L_{\text{screen}} \lambda} \ll 1, \quad (1.14)$$

with a the characteristic size of an aperture, L_{screen} the distance of a screen from an aperture, and θ_{\max} the maximal angle approximated by

$$\theta_{\max} \approx \frac{a}{L_{\text{screen}}}, \quad (1.15)$$

(Hecht 2017). For the slatted mirror M2 in the XRI set up shown in Figure 1.2, $a = w$ and $L_{\text{screen}} = L$. Substituting these substitutions and Equation 1.15 into Equation 1.14 gives

$$\frac{w^4}{4\lambda L^3} \ll 1. \quad (1.16)$$

The near field approximation will become the far field approximation (Fraunhofer diffraction) if the above expression were to approach or exceed the value of 1 (Hecht 2017).

The diffraction pattern uses the dimensionless coordinate u , defined as

$$u = y \sqrt{\frac{2}{\lambda L}}, \quad (1.17)$$

(Hecht 2017). The normalised Fresnel integrals are

$$C(u) = \int_0^u \cos \left(\frac{\pi \omega^2}{2} \right) d\omega, \quad (1.18)$$

and

$$S(u) = \int_0^u \sin\left(\frac{\pi\omega^2}{2}\right) d\omega, \quad (1.19)$$

with ω an integration parameter. The complex amplitude A is given by

$$A = C(u_2) - C(u_1) + i(S(u_2 - S(u_1)), \quad (1.20)$$

where $u_1 = u - \frac{u_0}{2}$, $u_2 = u + \frac{u_0}{2}$, and $u_0 = w\sqrt{\frac{2}{\lambda L}} = \sqrt{2N_f}$ (Willingale 2004), thereby $C(u_2) - C(u_1)$ is the Fresnel integral of Equation 1.18 from u_1 to u_2 . These two values of u are separated by a distance of w , translated to the dimensionless coordinate u . Given that u translates the y-position on the detector plane in a similar way, the Fresnel integrals integrate over the beam width on the detector plane that passes through the gaps. The diffraction caused by transmission through a narrow gap is identical to the diffraction caused by the reflection off of a slat with the same dimensions. The intensity of the diffraction pattern I_{diff} , can than be calculated as per

$$I_{\text{diff}} = AA^*, \quad (1.21)$$

with A^* the complex conjugate of the complex amplitude A .

Equation 1.21 gives the intensity of the Fresnel diffraction pattern for a single slat/gap and it is shown in Figure 1.3 for X-rays with a wavelength of 10 Å going through a gap, or reflecting of a slat at a distance of $L = 10$ m from the detector and with a projected slat/gap width $w = 300 \mu\text{m}$. Garde (2023), showed that for reasonable values of w , the diffraction patterns of all slat-gap pairs can be considered as independent, non-interacting and non-overlapping patterns next to each other. The entire diffraction pattern has an offset when the source is off-axis. As the flat mirrors conserve the angle change and the diffraction occurs at the slatted mirror (M2), the diffraction pattern is offset by $-L\theta$.

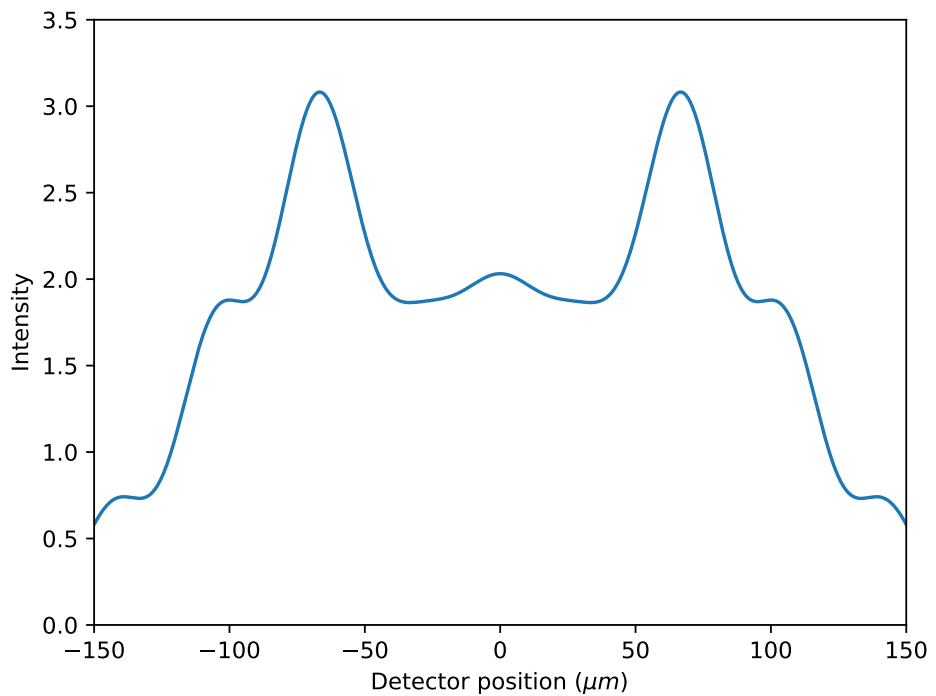


FIG. 1.3 – The intensity of Fresnel diffraction pattern for X-rays with a wavelength of 10 \AA going through a gap, or reflecting of a slat at a distance of $L = 10\text{ m}$ from the detector and with a projected slat/gap width $w = 300\text{ }\mu\text{m}$.

1.4 Simulator History

An end-to-end simulator of the proposed spacecraft is a very important tool in the current development stage. It can show scientists what is possible within mechanical limitations and inform engineers about the required tolerances. It is therefore both a tool to garner interest within the scientific community and a tool in the design process. This simulator was created by Emily van Hese in 2023, as part of her master thesis at the Anton Pannekoek Instituut, and named "XRImulator" ([van Hese 2023](#)). Her thesis goes into much further detail on how the simulator was built and how it functions. In this thesis the simulator will be corrected, improved and expanded upon.

Chapter 2

The Simulator

In this chapter the corrections, improvements and expansions of the simulator will be discussed. The structure of this chapter follows the current structure of the simulator. A schematic representation of the current structure is shown in Figure 2.1. All parts highlighted in green have been changed as part of this thesis and will be discussed in this Section. The structure and the modules remain roughly the same as they were. For a detailed overview of the unchanged parts and processes, see [van Hese \(2023\)](#). The simulator is an open access, object oriented, python code, consisting of four modules and an additional script for executing the desired functions of the simulator. Starting with the first ‘end’, the astrophysical source. It is sampled in the Image module, to generate photons. Secondly, the whole instrument is created in the Interferometer module. It consists of the main body, within which multiple baselines can be saved, and within each of those is a detector. Within the Process module, the sampled source photons go through the initialized interferometer, resulting in deduced photon properties (e.g. impact position, time of arrival (TOA) and energy). This is pre-processed data and not direct detector output data. The output from the detector will likely be a representation of the detected charge from specific pixels. This is related to and can be calibrated to photon energy and based on the pixels detecting certain amounts of charge, an impact location can be inferred. The readout time, by the computer system controlling the detector, is likely the assigned TOA. Converting direct detector output into inferred detected photon properties is still being researched and depends on the detector. This process has therefore been abstracted out and can be accounted for, using noise parameters. The collection of inferred photon properties can then be analysed, using different techniques for different purposes, in the Analysis module. A separate file is used to initialize and run the simulator, not further discussed in this thesis.

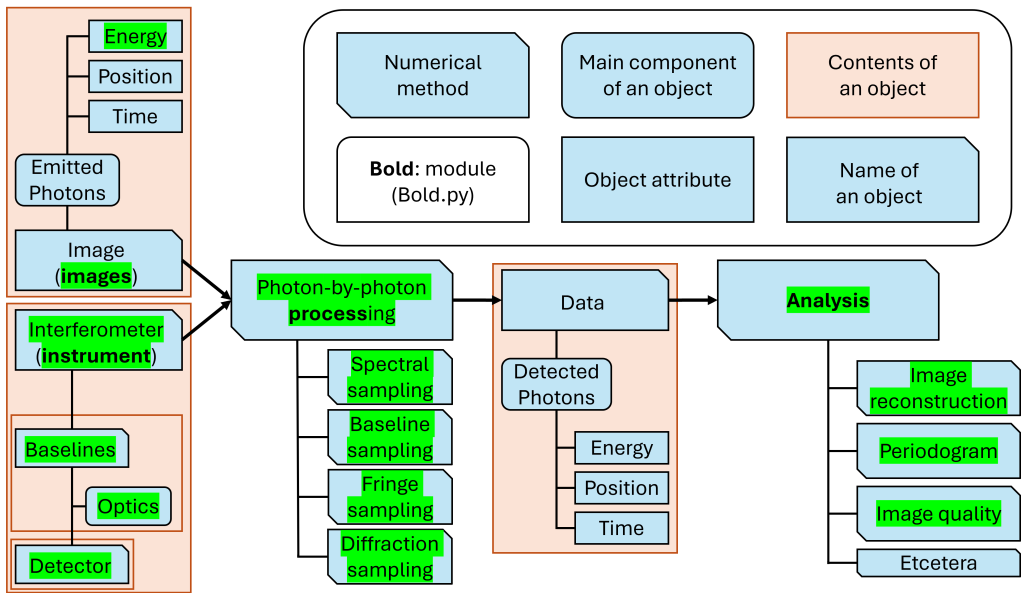


FIG. 2.1 – A schematic overview of the structure of the end-to-end simulator. A legend is given at the top left. Every highlighted part has been worked on during this thesis and is discussed below. The Figure shows how the image and interferometer objects have to be generated and fed into the processing method to obtain the data object, which can then be visualised and analysed by the analysis methods. Along with this structure, it highlights a few of the most important attributes and components of the separate parts of the code. The schematic structure has been adopted from [van Hese \(2023\)](#).

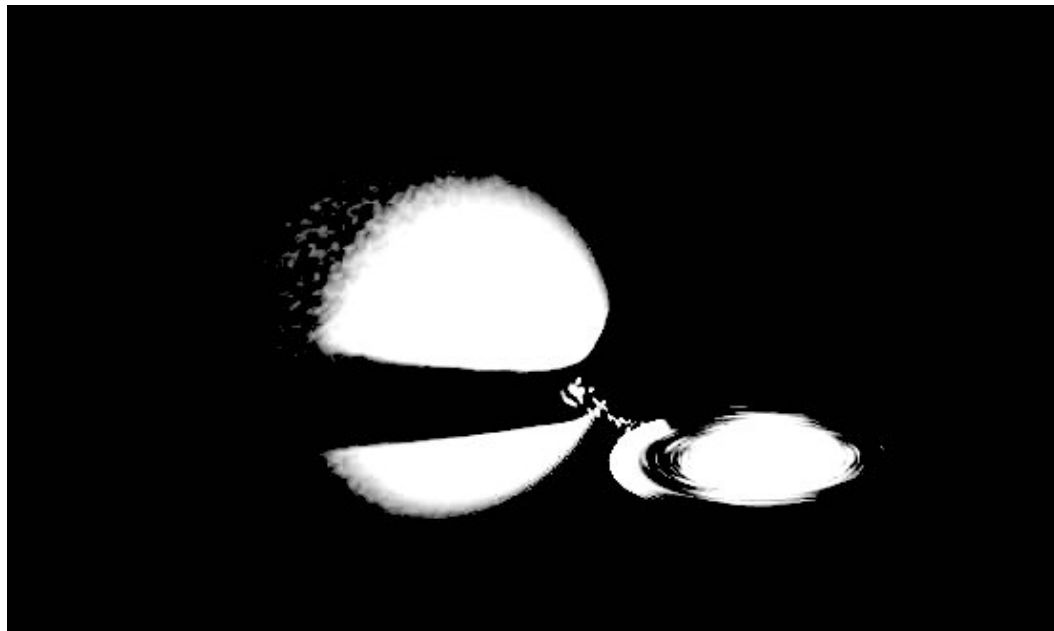


FIG. 2.2 – A model image of Cyg X-1, discussed in Section 1.2.1. Showing the BH accretion disk, the primary continuum source, to the right of the image. An illuminated disk rim and face of the companion star (with parts shadowed by the disk). The x-axis has an angular scale of $550 \mu\text{as}$, divided in 550 pixels. The y-axis is divided into 330 pixels, with square pixels. Adapted from a visualisation of a high mass X-ray binary by T. Russell and R. Hynes.

2.1 Images

The first ‘end’ of the end-to-end simulator is the astrophysical source. The simulator requires individual photons, including their properties, to be sampled from the source. These include the points of origin, TOAs, photon energies (or spectrum, see Section 2.1.1). The types of sources remain unchanged from [van Hese \(2023\)](#). The source photon energy (or spectrum) is independent of the point of origin in the current version of the simulator. The energy (or spectrum), thus, does not change for different points of the source.

This thesis uses three main astrophysical source model images: Cyg X-1, AU Mic and Sagittarius A* (Sgr A*). The input images for these sources are shown in Figures 2.2, 2.3, and 2.4, respectively.

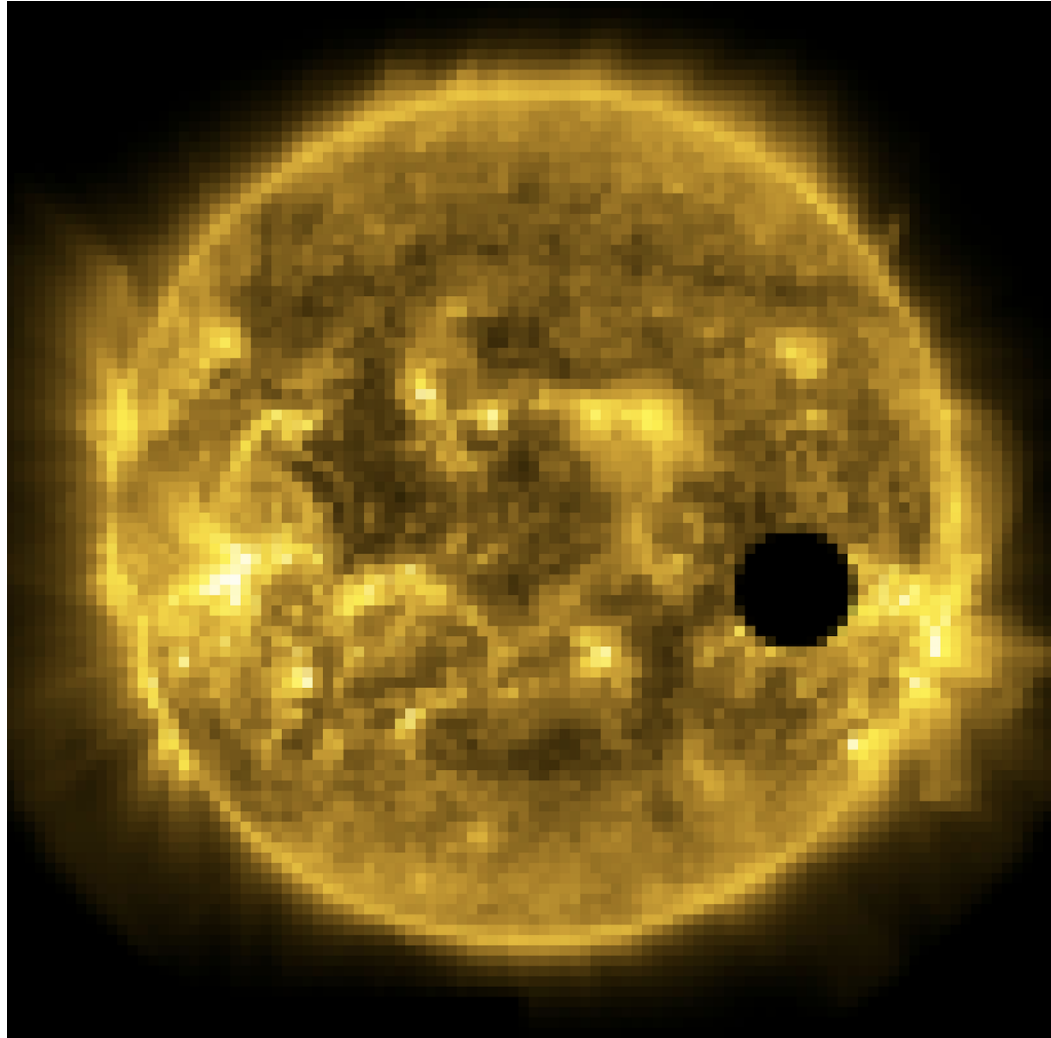


FIG. 2.3 – Assumed image of the corona of a low-mass star with a transiting exoplanet at 10 pc from the Sun, with an angular resolution of $10 \mu\text{as}$. This example uses the active solar corona (SDO AIA 171 band) as input, and assumes system parameters of the star and planet similar to the AU Mic system, discussed in Section 1.2.2. Adapted from [Uttley et al. \(2021\)](#).

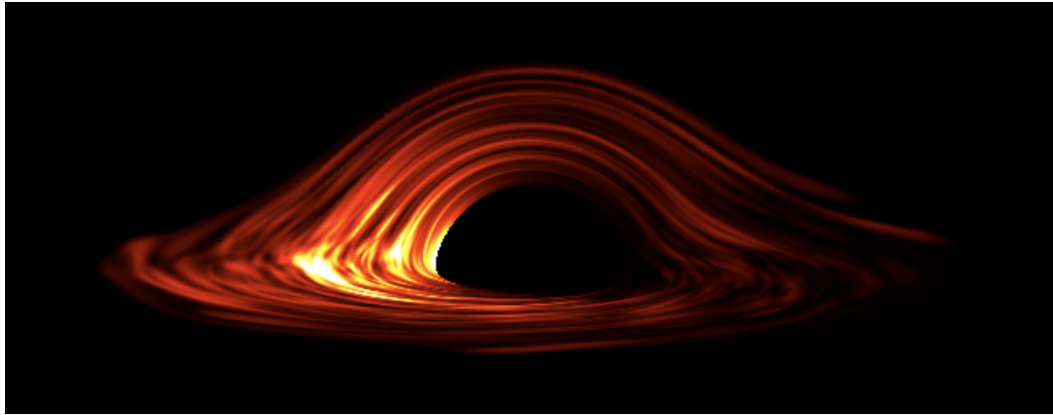


FIG. 2.4 – Simulated image of Sgr A*. The x-axis has an angular scale of $370 \mu\text{as}$ and with square pixels. The simulation is based on an image of a turbulent black hole accretion disk, based on the accumulation of 50-100 X-ray flares, totalling 10^5 counts. X-ray flaring is likely to be produced by synchrotron emission in the hot radiatively efficient flow (Ponti et al. 2017), but may be Doppler boosted by rotation of the flow to produce an image similar to the one shown. Adapted from Uttley et al. (2020).

2.1.1 Spectra

All astrophysical source models, where relevant, are expended to include a spectrum parameter. This can either be a file name, or a calculated input spectrum. The input is then converted to the desired format. The simulator returns an error when neither a source energy, nor a spectrum is given. If a source spectrum is supplied, the photon energies are sampled in the Process module. When no energy spectrum is supplied, the photon energies will be set in the Image module. This can either be for a monochromatic case, or when there is a Gaussian energy spread given.

2.1.2 Background

For the case where an input image is sampled as a source, there is now the option to add a background. This is a uniform background over all pixels of the input image. The background can either have a monochromatic energy, or a spectrum. All background photon energies are sampled from the same monochromatic energy or energy spectrum. When neither the background spectrum, nor the energy are given, the background photon energies are assumed to be the same as the source photon energies. In the case that only a source spectrum is given, the background photon energies are set to be the unweighted mean energy of the source spectrum. If the background spectrum is given, without a background energy, the background energy is set to the unweighted mean energy of the background spectrum. Currently the background spectrum is not yet sampled in the Process module, thus the given or

Images

calculated energy is used. Figure 2.5 shows the point of origin sampling of the Cyg X-1 model image, shown in Figure 2.2. The top panel shows only source counts, the middle panel shows equal source and background counts, and the bottom panel shows only background counts. Equal source and background counts is unrealistic for Cyg X-1. It is used for demonstrating the functionality for potential fainter sources of interest. The effects of this background is discussed in Section 3.2 and shown in Figure 3.2.

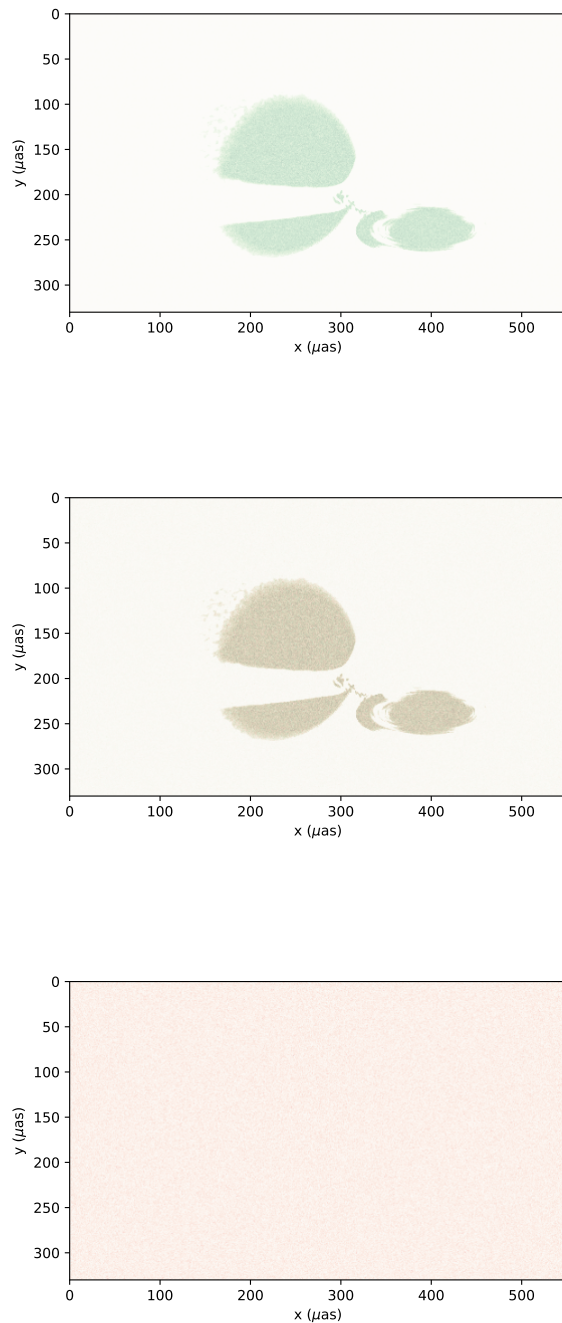


FIG. 2.5 – The sampling of the model image of Cyg X-1. Showing only source counts, equal source and background counts, and only background counts. The source and background are both sampled to have 10^6 photon counts. Therefore the middle panel consists of 2×10^6 total photon counts.

2.2 Instrument

The whole instrument is created in this module. It consists of the main body, within which multiple baselines can be saved, and within each of those is a detector. The current full spacecraft concept is shown in Figure 2.6. The shown components of the attitude and orbit control system control loop (star trackers, ring-laser gyroscopes, cold-gas microthrusters and the flight systems) and their effects are not included in the current version of the simulator. Preliminary versions of spacecraft wobble are implemented ([van Hese 2023](#)). The spacecraft in the simulator consists of three parts: the main body, the baselines and the detectors. Each being nested in the previous object.

2.2.1 Main body

The main class of the interferometer, inside of which the baselines are saved. With the detectors being saved within the baseline classes. With the detector becoming a separate class, the energy resolution, time resolution, positional resolution, energy range and positional range parameters have been moved to the detector class.

Two new parameters have been introduced. The maximum length of the optics and the maximum weight of the optics. These can be used to check whether the designed set up fits the requirements, shown in Figure 2.6.

2.2.2 Baselines

The baselines class defines the optical bench, according to the design discussed in Section 1.3.1. It now takes all parameters of that design as input values. Those that are not given are calculated where possible. If the given parameters are not self-consistent, according to the equations, the simulator returns an error. The same happens when essential parameters cannot be calculated due to missing key parameters. This allows for improved versatility and freedom for an expert user, while maintaining simplicity for the average user. The baselines are now compatible with parameter searches to optimise the parameters of the optical design. Simultaneously, the simulator can be used to investigate science cases, while requiring only limited understanding of the intricacies of the design. One new key parameter is the number of slat-gap pairs (N_{pairs}) in the slatted mirror (M2).

Additionally the baseline class now accepts the bench length, and the interferometer class, of which it is a part. This allows for testing the length requirements shown in Figure 2.6. This is mainly important for the parameter searches mentioned above, as the final spacecraft must remain within launchable parameters.

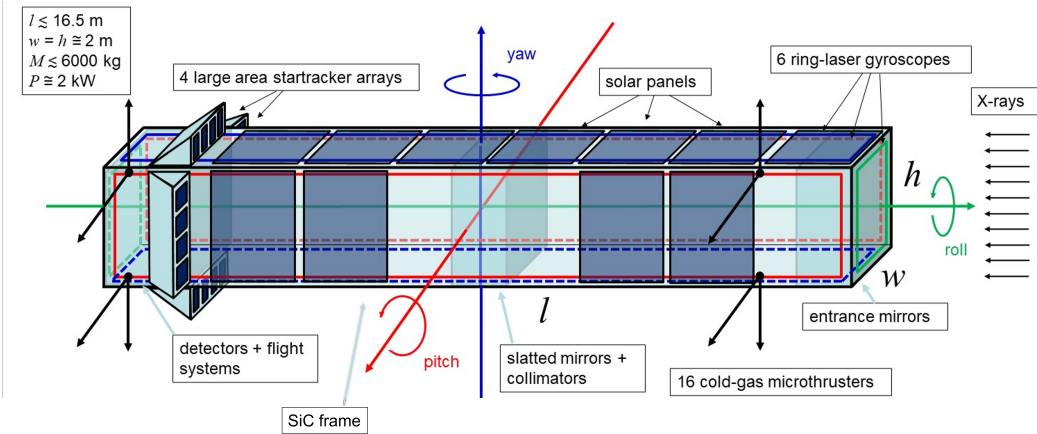


FIG. 2.6 – The spacecraft carrying XRIs, as currently envisioned. It shows the different components of the attitude and orbit control system: four large star tracker arrays, six ring-laser gyroscopes, 16 cold-gas microthrusters and the flight systems. The ring-laser gyroscopes register the 3 pointing angles (pitch, yaw and roll). The power generation, equivalent to the maximum available power for operations, through the solar panels is estimated to be $P \cong 2 \text{ kW}$. The frame is expected to be made out of silicon carbide (SiC), to keep the mass under $m \leq 6000 \text{ kg}$ and to ensure sufficient rigidity for launch with an Ariane 64 launch vehicle (Lagier 2021). Finally the parts of the optical benches are included: the collecting (here entrance) mirrors, the combining (here slatted) mirrors, collimators (against stray light) and the detectors. The dimensions of the spacecraft: total length $l \leq 16.5 \text{ m}$, width and height (excluding the star trackers) $w = h = 2 \text{ m}$. Note that these parameters do not directly correlate with any other parameters used elsewhere in this thesis, especially l and w used here should not be confused with L , W and w used elsewhere. These dimensions will allow the spacecraft to fit within the extended fairing of an Ariane 64 launch vehicle (Lagier 2021). Figure courtesy of Roland den Hartog.

The baseline class now also accepts mirror reflectivity. These are assumed to be files generated by an online tool¹ which calculates X-ray reflectivity and transmission. Alternatively, the reflection can be calculated elsewhere and provided in the same layout. Using the aforementioned tool, Figure 2.7 shows the reflectivity of pure silicon mirrors as a function of photon energy (in keV), for different θ_g . It is clear that there is barely any reflectivity at higher energies, with the exception of $\theta_g = 0.01^\circ$. Therefore the eventual mirrors in the spacecraft will likely be made of silicon with an iridium coating, similar to the mirrors of (New)Athena (Svendsen et al. 2019). Note the reported reflectivity performance (Figure 1 in Svendsen et al. 2019, see Figure A.1) at higher photon energies for iridium, when compared to pure silicon shown here in Figure 2.7. While iridium offers good reflectivity across the energy range, the addition of silicon is critical to improve the low-energy performance (Svendsen et al. 2019).

When combining the mirror reflectivity with the quantum efficiency of the detector, further discussed in Section 2.2.3, the effective area can be calculated. The maximum effective area A_{Eff} is calculated as

$$A_{\text{Eff}} = \frac{1}{12} S R^2 Q, \quad (2.1)$$

with S the the aperture area, R the mirror reflectivity and Q the detector quantum efficiency and where both R and Q are energy dependent (Uttley et al. 2020). The factor R^2 comes from the double reflection of the beam required in the optical setup shown in Figure 1.2. The factor $\frac{1}{12}$ comes from the total area of the collecting mirrors not exceeding a quarter of the available area for the spacecraft aperture (due to stack spacing requirements, Uttley et al. 2020) and an assumed fractional photon admittance of a third by the M2 mirror (Willingale 2004). An example of a single baseline effective area is shown in Figure 2.8. This was calculated using Equation 2.1. Where R was obtained with a grid interpolation on the data from Figure 2.7, evaluated at $\theta_g = 0.9^\circ$ and the shown energy range. Where Q was obtained with a one dimensional interpolation of the data from Figure 2.7, evaluated at the shown energy range. The step function like behaviour is a result from the grid interpolation, using the ‘nearest’ method. A significant decrease of A_{Eff} , compared to S , is apparent. One caveat is the assumption $S = w^2$ in calculating A_{Eff} . This is a conservative estimate, with $S = w \times h_{\text{beam}}$ being more accurate and the height of the beam $h_{\text{beam}} > w$. Regardless A_{Eff} , will likely remain small for a single baseline. To combat this, Willingale (2004) suggested using many slat-gap pairs, where $S \propto N_{\text{pairs}}$. An additional solution is parallelization, as suggested by Uttley et al. (2020). The latter solution can be applied in the simulator by adding manual copies of the same baseline classes.

The quantum efficiency of the detector is a part of the detector specifications, saved in the new detector class. A standardised detector is defined during the initialization of the Baseline class and saved within. To allow for changing the detector to the

¹<https://henke.lbl.gov/>

desired specifications, a new function is added. This results in each baseline having its own unique detector, thus allowing for the ability to optimise detectors for each baseline. It also opens up the possibility to incorporate future detector response matrices, further discussed in Section 2.2.3.

Another new function in the baseline class is a function which returns a change in the path lengths at given times. The times here would be the actual real arrival times of the photons. Currently this function always returns a difference of 0 m. In the future this function can incorporate and interpolate output data from simulations of effects which effects the stability of the path lengths (e.g. thermal fluctuations). Doing the path length perturbation simulations outside of the simulator, the computational time will remain low. This is due to the fact that the perturbation simulations will only be run once, as they remain constant for each run of the simulator (assuming no change in the perturbation effects, other then time variability).

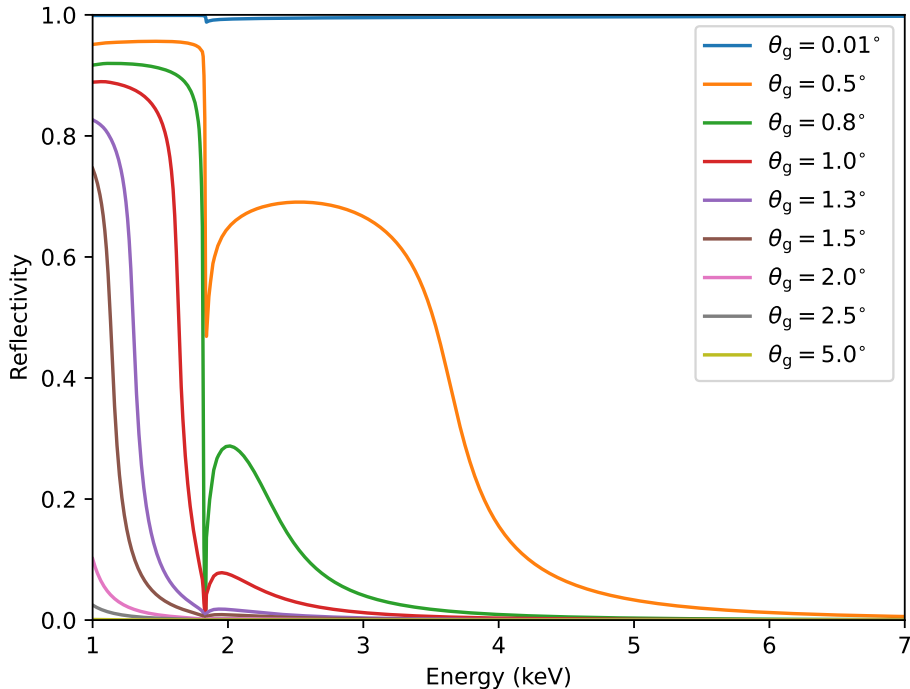


FIG. 2.7 – The mirror reflectivity as a function of photon energy in keV. This Figure shows the reflectivity, compared to unity, of the testing mirrors planned to be used in lab experiments of an XRI. These mirrors are made of silicon. The energy range is chosen to encompass the region of interest for the space mission. The data was gathered using an online tool¹ for calculating X-ray reflection and transmission.

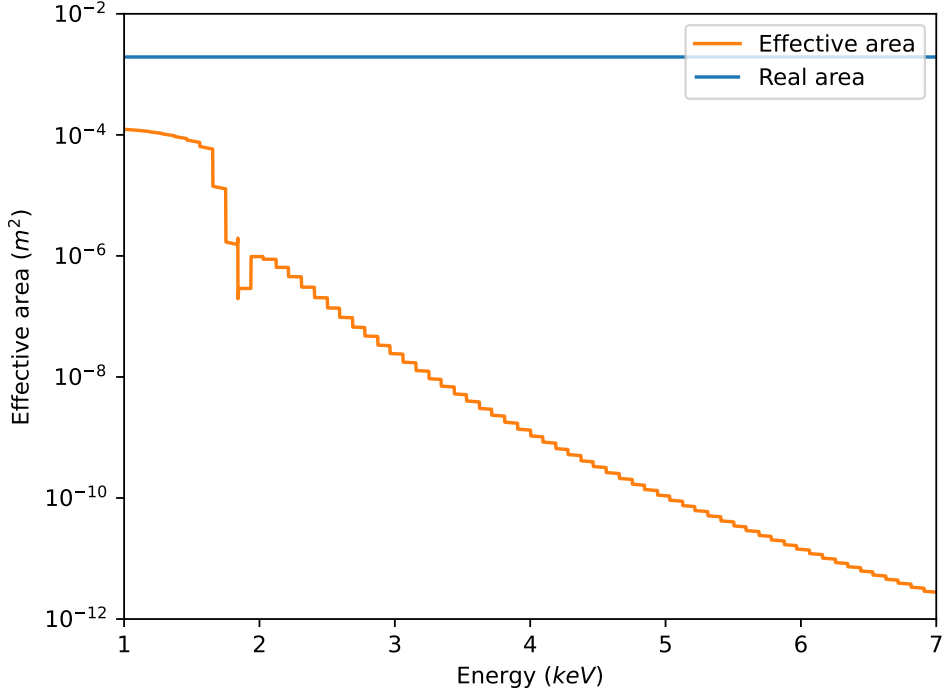


FIG. 2.8 – The effective area as a function of photon energy in keV, including the real aperture area for reference. This Figure shows the effective area of a single baseline optical set up, similar to planned lab experiments of an XRI. The energy range is chosen to encompass the region of interest for the space mission. The results shown are based on data gathered using an online tool¹ for calculating X-ray reflection and transmission. Here a grazing angle $\theta_g = 0.9^\circ$ is used.

2.2.3 Detector

A new class was added: the detector class. This was previously nested in both the Process and Analysis modules. Extracting it allows for testing without detector effects present, thus allowing for better understanding the impact of the detector effects. The detector class requires energy resolution, time resolution, positional resolution, energy range and positional range. These are set by a detectors specification. Additional arguments can be given for the positional noise, energy noise, time noise, quantum efficiency and response matrix.

The noise parameters are used to shift the recorded data with respect to the real values. The resolutions in combination with the ranges are currently used to pixelate these values to a grid. This is done by dividing up the respective ranges in an integer number of bins, whose width is set equal to the respective resolution. Then the real values are all shifted to the centre of their respective bins.

A response matrix encodes the energy dispersion and calibration of incoming photons

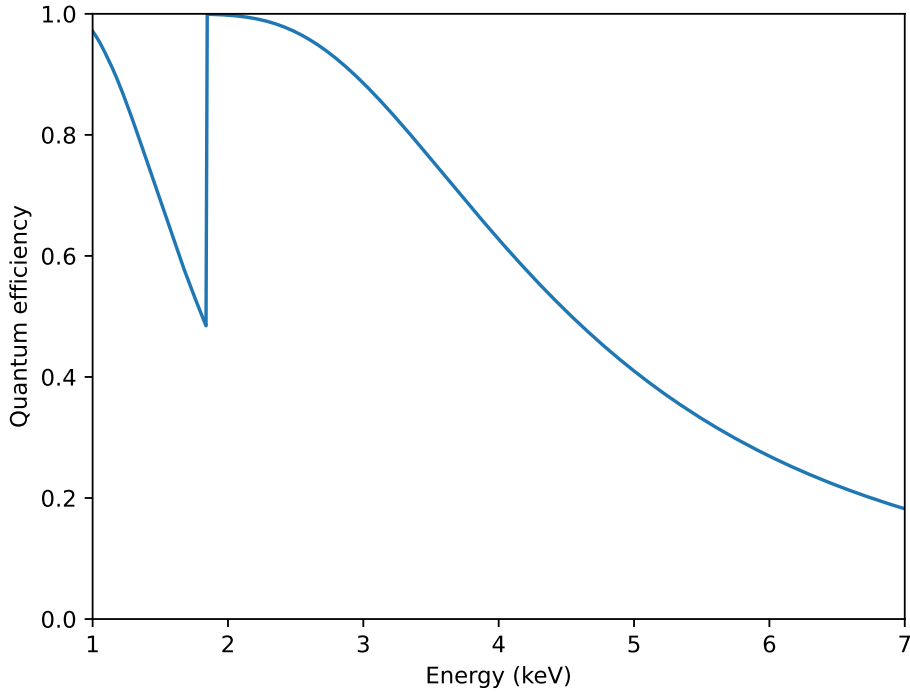


FIG. 2.9 – The detector quantum efficiency as a function of photon energy in keV. This Figure shows the absorption, compared to unity, of the testing detector currently used in lab experiments of an XRI. The energy range is chosen to encompass the region of interest for the space mission. The data was provided by Aditya Garde using an online tool¹ for calculating X-ray reflection and transmission, from which the absorption can be calculated as the remainder.

at different energies to recorded energy channels. It also encodes the effective area of the detector as a function of energy for a given incoming angle. Given the small angle difference between incoming photons, on the order of θ_b , the effective area is likely independent of θ . The effects of a response matrix have not yet been implemented. Once it is, it would take over the need for the detector quantum efficiency. The detector quantum efficiency is set by the detector specifications and determines the effective area of the detector, when combined with the physical detector area, as a function of energy. The quantum efficiency of a testing detector currently used in the lab experiments of an XRI are shown in Figure 2.9. The data was provided by Aditya Garde using an online tool¹ for calculating X-ray reflection and transmission, from which the absorption can be calculated as the remainder. The lab tests remain in the lower energy range of this plot, the future spacecraft will require higher quantum efficiency at higher energy range.

2.3 Process

Within this module, the sampled source photons go through the initialized interferometer, resulting in deduced photon properties (e.g. impact position and energy). This is pre-processed data and not direct detector output data. If an image spectrum is given, the photon energies are sampled. Sampling image spectra in this module allows for retaining the simulator structure of [van Hese \(2023\)](#). With the photon energies and points of origin, the pattern on the detector (see Section 1.3.2) is sampled and baselines are selected. All detector effects, through parameters and functions, are moved to the new detector class (see Section 2.2.3).

2.3.1 Energy sampling

A new function is added to sample image spectra. It takes the initialized interferometer and the sampled image as main input parameters. It has an additional toggle to show the calculated A_{Eff} of all baselines, discussed in Section 2.2.2. An example of photon energy sampling from a source energy spectrum, unmodulated by A_{Eff} , is shown in Figure 2.10. The input spectrum was measured using the Low Energy Transmission Grating (LETG) gratings of the Chandra X-ray Observatory and the spectrum shown here has already been corrected for the instrument response. The spectrum is the source spectrum, before a type-I thermonuclear burst, of the source SAX J1808.4-3658 (ObsID 13718), provided by Noud Hover. Including the baseline's A_{Eff} modulation effects, shown in Figure 2.8, results in the sampling shown in Figure 2.11. Note the lack of photons at higher energies. While the source spectrum and A_{Eff} are continuous over energy, the photons are discrete. The bar at the sampled photon energy $E_{\text{phot}} \approx 5.2 \text{ keV}$, consists of a single photon event. The probabilities for photon energies $E_{\text{phot}} \gtrsim 4 \text{ keV}$ become fractions of a count, given this example at 10^5 sampled photons, thus resulting in the lack of photons in this region and the bad matching between the sampled energy distribution, from the input distribution. The energy sampling makes use of inversion sampling, also known as inverse transform sampling. When starting with a continuous distribution, which is achieved here through interpolation, it can be normalized to create a probability density function (pdf). From this pdf, a cumulative density function (cdf) can be calculated using

$$F_X(x) = P(X \leq x), \quad (2.2)$$

with $F_X(x)$ the cdf and $P(X \leq x)$ the probability that the random variable X takes on a value less than or equal to x . The y-value of the cdf will go from 0 to 1, over the x-range of the original distribution function. Taking a random uniform variable $U \in [0, 1]$ as an x-coordinate, for the inverse of the cdf, gives a y-value corresponding to the sampled photon energy.

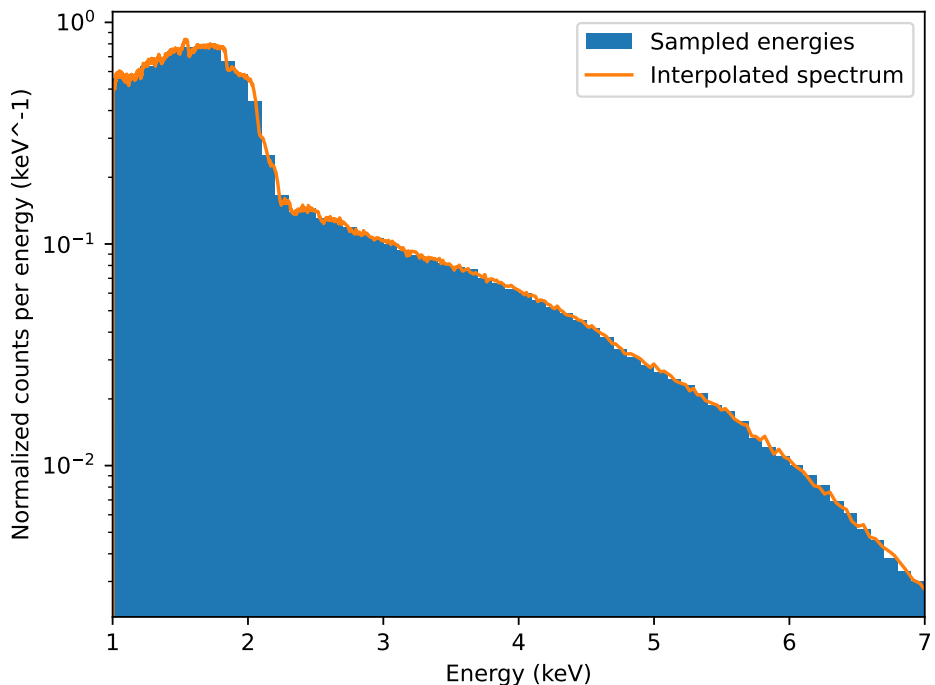


FIG. 2.10 – An example of spectral energy sampling. The normalized source counts per energy (keV^{-1}) are plotted against energy (keV). The energy range is chosen to encompass the region of interest for the space mission. The histogram in blue represents the normalized sampled energy counts. The orange line is the interpolated spectrum, used for sampling the energies. This spectrum is sampled using 10^5 photon counts. The input spectrum was measured using the LETG gratings of the Chandra X-ray Observatory and the spectrum shown here has already been corrected for the instrument response. The spectrum is the source spectrum, before a type-I thermonuclear burst, of the source SAX J1808.4-3658 (ObsID 13718), provided by Noud Hover.

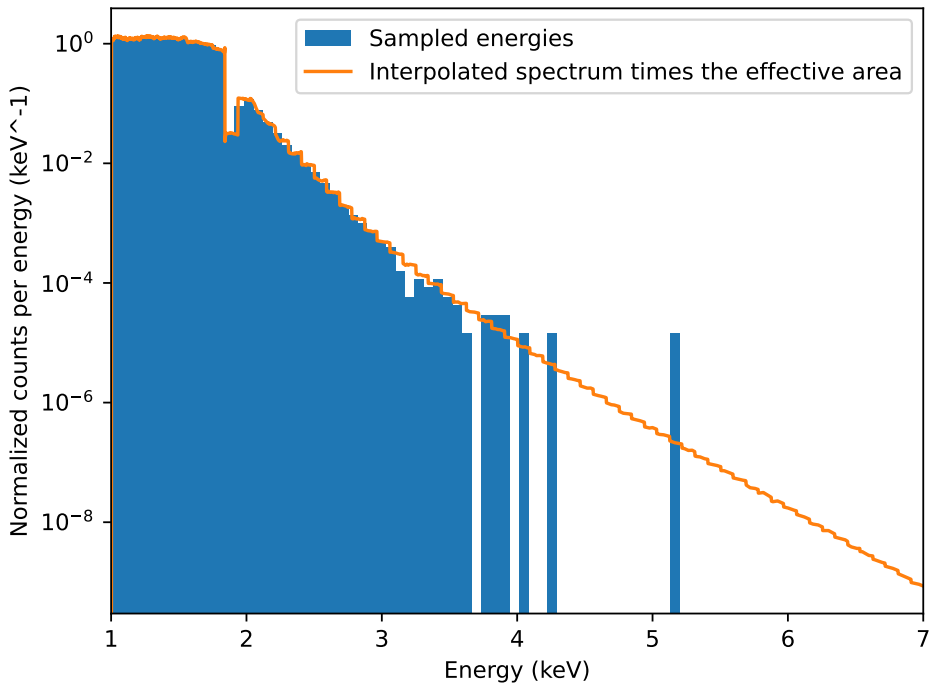


FIG. 2.11 – An example of spectral energy sampling, when also accounting for the energy dependence of A_{Eff} . The normalized source counts per energy (keV^{-1}) are plotted against energy (keV). The energy range is chosen to encompass the region of interest for the space mission. The histogram in blue represents the normalized sampled energy counts. The orange line is the interpolated spectra multiplied with A_{Eff} , used for sampling the energies. This spectrum is sampled using 10^5 photon counts. The effective area used, is the one shown in Figure 2.8. The input spectrum is the one shown in Figure 2.10, provided by Noud Hover.

2.3.2 Baseline selection

The energy sampling discussed above requires the A_{Eff} of a baseline. As discussed in 2.2.2, this can vary between baselines. Therefore, the energy sampling function also samples which baseline a photon goes in. Previously, the baseline selection was done randomly based on a uniform distribution (van Hese 2023). This does not take into account possible differences in A_{Eff} , which effects the likelihood of a photon being detected in a certain baseline. This is solved by calculating the theoretical number of photon counts per baseline, using

$$\int N(E)A_{\text{Eff}}(E)dE, \quad (2.3)$$

with $N(E)$ the photon count ($\text{cm}^{-2} \text{s}^{-1} \text{keV}^{-1}$), over the entire detectable energy range. The baselines are then selected based on their theoretical photon counts as a fraction of the total number of counts, resulting in a probability for a photon to be detected in a specific baseline.

2.3.3 Pattern correction

It was previously understood that both the fringe and diffraction patterns shift with $\sim -F\theta$. This follows from the equations in Willingale (2004), but are in stark contrast with the findings in Figure 7 of the same paper. The simulator must therefore be updated to the current understanding of the total pattern discussed in Section 1.3.2. The equations in Willingale (2004) allow for a simple and fast exact calculation of the probability distributions as a function of position on the detector, from which the exact photon impact positions can be sampled. This is no longer the case when the fringe and diffraction patterns have a different θ dependent shift.

To sample the fringe pattern, a cosine distribution is used to sample a single fringe. The sampled fringe has a width equal to the fringe spacing (calculated using Equation 1.2) and is centred at the centre of the left most fringe, (partially) visible within the total diffraction pattern. Each slat-gap pair has an individual diffraction pattern of width w . The total diffraction pattern has a width of $N_{\text{pairs}} \times w$. The centre of the fringe pattern is calculated using Equation 1.11. Combining the total width of the pattern on the detector, with the position on the detector of the central fringe and the fringe spacing, the centre of the left most fringe (partially) visible within the total diffraction pattern is calculated. From there a random positive integer is taken between, and including, 0 and N_f to distribute the photons over all (partially) visible fringes, thereby sampling the full fringe pattern.

The next step is to use the accept-reject method to sample the diffraction pattern. The accept-reject method makes use of a random x-value, for which the exact value of the desired distribution is calculated. In the implementation here, the random

x-values are provided by the sampled fringe pattern described above. Then a random y-value is generated, based on a predefined box around the desired distribution. If the random generated y-value is smaller or equal to the exact calculated y-value for the corresponding x-value, the x-value is accepted and saved. Otherwise the point is rejected. This process is repeated until the desired number of sampled points has been accepted. The random x- and y-value ranges are set by the chosen box. The ratio of the area under the desired distribution to the area of the box is equal to the ratio of accepted points to the number trials (known as the acceptance rate). The more precisely the defined box matches the desired distribution, the larger this ratio and the faster and more computationally efficient the method is. Due to the variability of the Fresnel diffraction pattern as a function of the photon energies and the slatted mirror parameters, it is difficult to define a well fitting fair box. Therefore, a simple rectangular box is used with a width equal to that of the total diffraction pattern of $N_{\text{pairs}} \times w$. A separate calculation showed that the ratio between the central value of the diffraction pattern to the maximum of the same diffraction pattern never exceeds 2.7. Therefore the height of the box is calculated as 2.7 times the height of the diffraction pattern at its centre, given the specific diffraction pattern for each individual photon. Though this is far from an optimised box, the acceptance rate lies between $\sim 15\%$ and $\sim 60\%$ (for most realistic cases $\sim 30\%$ and $\sim 50\%$). Though this is not ideal, it is sufficient, especially when considering that defining a very specific box itself can also become computationally intensive. An acceptance rate of 100% is never expected using the accept-reject method and generally a decrease of computational time by a factor of ~ 4 or more is considered significant.

A very important point in the application of the accept-reject method here is that both the accepted and rejected photons retain their respective properties. Only the aforementioned sampled detector position trial of the rejected photons is repeated. This also includes their relative positions in the arrays, as those are implicitly connected to the order of detection. Losing this order results in a disconnect between the spacecraft rotation and fringe pattern. This is catastrophic for image reconstruction. By also saving the photon properties, the source image does not require resampling. This reduces computation time, retains the simulator structure (as per [van Hese 2023](#)), and does not affect the statistics.

Figure 2.12 shows the sampled photon counts of the pure fringe pattern. The vertical orange line shows the shift of the central fringe. The absolute shift is in agreement with Equation 1.11 for a monochromatic photon energy $E_{\text{phot}} \approx 1.2 \text{ keV}$, the XRI parameters used by [Willingale \(2004\)](#) with only two slat-gap pairs, and an off-axis angle $\theta = 0.9 \text{ mas}$. Figure 2.13 shows the sampled photon counts of the pure Fresnel diffraction pattern. The vertical red line shows the center of the diffraction pattern. All parameters, with the exception of the off-axis angle θ , are the same as in Figure 2.12. Note the change of x-axis values, the observed shift is in agreement with a diffraction patterns shift of $L\theta$. Figure 2.14 shows the sampled photon counts of the full pattern. The vertical orange and red lines shows the central fringe and the center of the diffraction pattern, respectively. All parameters, including the off-axis

angle θ , are the same as in Figure 2.12. The fringes clearly shift within the diffraction pattern envelope. The diffraction pattern shift is significant when $\text{FoV} \times L$ is significant with respect to Δy . Given the design parameters discussed in Willingale (2004), the diffraction pattern shift is only significant when the central fringe is outside of the FoV. This happens when the central fringe is outside of the diffraction pattern envelope and thus not visible on the detector.

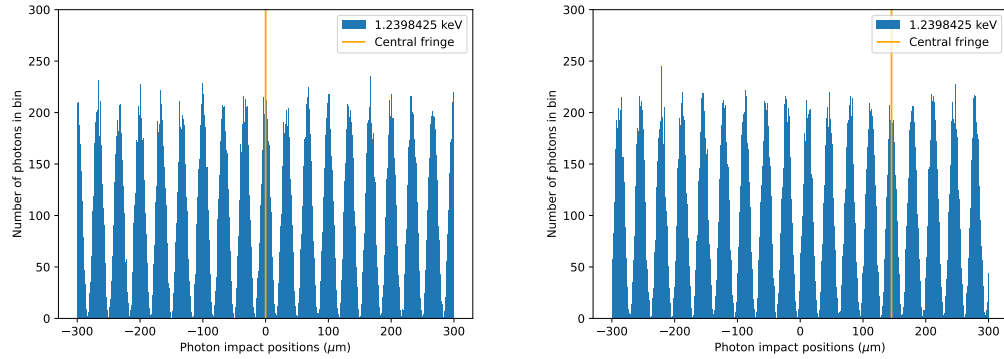


FIG. 2.12 – Both Figures show the sampled photon counts per positional bin against the detector impact positions for a pure fringe pattern. Both Figures use a monochromatic photon energy $E_{\text{phot}} \approx 1.2 \text{ keV}$, 10^5 total counts and an XRI based on the parameters used by Willingale (2004) with only two slat-gap pairs. The left Figure shows an on-axis point source, thus with an off-axis angle $\theta = 0 \text{ as}$. The right Figure shows an off-axis point source, with an off-axis angle $\theta = 0.9 \text{ mas}$.

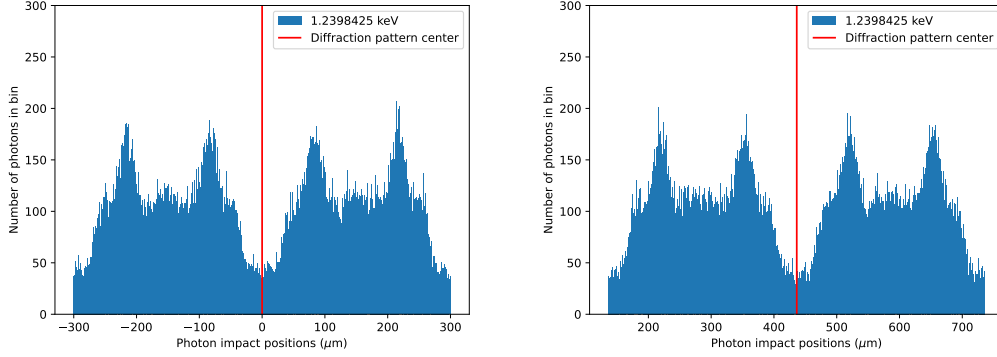


FIG. 2.13 – Both Figures show the sampled photon counts per positional bin against the detector impact positions for a pure Fresnel diffraction pattern. Both Figures use a monochromatic photon energy $E_{\text{phot}} \approx 1.2 \text{ keV}$, 10^5 total counts and an XRI based on the parameters used by [Willingale \(2004\)](#) with only two slat-gap pairs. The left Figure shows an on-axis point source, thus with an off-axis angle $\theta = 0 \text{ as}$. The right Figure shows an off-axis point source, with an off-axis angle $\theta = 9 \text{ as}$.

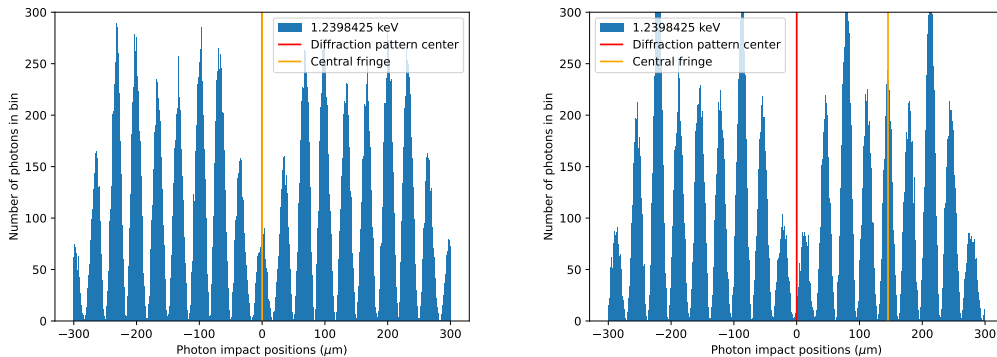


FIG. 2.14 – Both Figures show the sampled photon counts per positional bin against the detector impact positions for the full pattern. Both Figures use a monochromatic photon energy $E_{\text{phot}} \approx 1.2 \text{ keV}$, 10^5 total counts and an XRI based on the parameters used by [Willingale \(2004\)](#) with only two slat-gap pairs. The left Figure shows an on-axis point source, thus with an off-axis angle $\theta = 0 \text{ as}$. The right Figure shows an off-axis point source, with an off-axis angle $\theta = 0.9 \text{ mas}$.

2.4 Analysis

Within this module the deduced photon properties (e.g. impact position, TOA and energy) are analysed. Different techniques are used for different purposes. These include, but are not limited to, image reconstruction, periodograms, and image quality calculations. The former has been significantly changed and improved. The latter two are new additions to the module. All three are discussed below.

2.4.1 Image reconstruction

The image reconstruction function is the main feature of the Analysis module. It converts the deduced photon properties into a reconstructed version of an observed source. Each detected photon carries information of the source object from which it came. For this information to be extracted using interferometry, at least one detected photon is needed per energy and per origin coordinate on the sky, assuming only perfect source photon detections ([Uttley 2024](#); [Sriramanathan 2024](#)). The simulator used to bin the detected photons based on which baseline they were detected in, their energy, and roll angle ([van Hese 2023](#)). The energies were binned, based on the detector resolution. The roll angles were binned based on a user provided number of roll bins. Fewer bins result in more photons per bin, which leads to a higher signal to noise ratio (SNR), while more bins result in sampling more uv-coordinates, which results in more spatial information of the source being sampled ([van Hese 2023](#)). All bins with less than 10 photons were discarded to avoid added noise from insufficiently sampled fringes. The required number of photons was chosen empirically and could be set to 1.

By separating out the detector into its own class, the energies are no longer discretized based on the detector resolution. Instead, it would be possible to bin the energies based on all uniquely occurring energies. This becomes extremely computationally intensive when moving from a monochromatic source to one with an energy spectrum, as most photons have a unique energy. To slightly increase the computational efficiency the roll bins can be removed. This results in each photon position and energy contributing its own complex Fourier component at a (potentially) unique uv-coordinate. This is possible, because the Fourier transform of the sum of the photon positions (full pattern / distribution, see Figure 2.14) is mathematically equivalent to the sum of the Fourier transforms of all individual photon positions given their respective energies. The Fourier component and uv-coordinate calculations remain unchanged from [van Hese \(2023\)](#). These are then all inverse Fourier transformed using the inverse Fourier transform equation for each Fourier component and uv-coordinate combination, we call this method the exact inverse Fourier transform (eIFT) method. It is further sped up using a computer architecture called multithreading. This allows for calculating multiple Fourier component and uv-coordinate combination simultane-

ously and adding to the same final reconstructed image. Despite these improvements to the computational efficiency, the reconstruction times (of sources with spectra) remain long.

Faster methods for calculating, an approximated, inverse Fourier transform exist. This method is aptly named the inverse fast Fourier transform (IFFT) method. This method works with regularly spaced and ordered frequencies, allowing the positions of the Fourier components to implicitly be correlated to their respective uv-coordinates. Note that the uv-plane is the frequency domain of the corresponding image, the latter being in the spatial domain. In order to use the IFFT method, the exact uv-coordinates need to be mapped to the implicit frequencies used by the IFFT method. The frequencies are $f = [0, 1, \dots, n/2-1, -n/2, \dots, -1]/(d \times n)$ if n (the window length) is even and $f = [0, 1, \dots, (n-1)/2, -(n-1)/2, \dots, -1]/(d \times n)$ if n is odd, with d the sample spacing (inverse of the sampling rate, i.e. pixel size on the reconstructed image). This applies for both u and v , such that the very first value (top left) is the zero frequency term. The Fourier value of that pixel is the Fourier transform of the average pixel value of an image in the spatial domain. For given values of n and d , this results in a frequency grid. The exact uv-coordinates are mapped to this grid based on the closest frequency for both directions. The Fourier components of uv-coordinates that are mapped to the same frequency grid point are summed. The grid of the summed Fourier components is then inverse Fourier transformed using the IFFT method. The values of n and d must be chosen carefully. The computational complexity of a two dimensional IFFT is well understood to be $O(n^2 \log_2(n))$. This is to say that if n increases by a factor of 4, the computational time would increase by a factor 32. The smaller the value of n , the faster the method. The values of n and d are tied to the frequency grid, to which the exact uv-coordinates are mapped. They thus impact how good the approximate frequencies match to the exact uv-coordinates. The frequency bin width Δf is given by

$$\Delta f = 1/(d \times n). \quad (2.4)$$

The smallest sampled frequency is given by

$$f_{\text{samp, min}} = \frac{D_{\min}}{\lambda_{\max}}, \quad (2.5)$$

with $f_{\text{samp, min}}$ the smallest sampled frequency (with $f_{\text{samp}} = \sqrt{u^2 + v^2}$), D_{\min} the smallest used baseline of the XRI in meters and λ_{\max} the largest detected photon wavelength in meters. Any sampled frequency should be shifted by no more than a fraction of its frequency. To make ensure this for all frequencies, the smallest sampled frequency should be bigger then the maximum frequency shift $\frac{\Delta f}{2}$, thus,

$$\frac{\Delta f}{2f_{\text{samp, min}}} \geq \epsilon, \quad (2.6)$$

with ϵ the user provided maximum allowed fractional frequency shift. Using Equations 2.4 and 2.6, this can be rewritten as

$$n \geq \frac{1}{2d\epsilon \frac{D_{\min}}{\lambda_{\max}}}. \quad (2.7)$$

Additionally, the frequency grid must encompass the largest sampled frequency, given by

$$f_{\text{samp, max}} = \frac{D_{\max}}{\lambda_{\min}}, \quad (2.8)$$

with D_{\min} the largest used baseline of the XRI in meters and λ_{\min} the smallest detected photon wavelength in meters. The maximum frequency grid point $f_{\text{grid, max}}$ is given by

$$f_{\text{grid, max}} = \frac{n}{2} \Delta f, \quad (2.9)$$

if n is even and

$$f_{\text{grid, max}} = \frac{n-1}{2} \Delta f, \quad (2.10)$$

if n is odd. Thus, to ensure the maximum sampled frequency is encompassed by the frequency grid, $f_{\text{samp, max}} \leq f_{\text{grid, max}}$. Using Equations 2.4, 2.8, and 2.10, this can be rewritten as

$$d \leq \frac{n-1}{2n \frac{D_{\max}}{\lambda_{\min}}}, \quad (2.11)$$

where Equation 2.10 is used instead of Equation 2.9. This is because Equation 2.10 results in a lower upper bound for d (otherwise $d \leq \frac{1}{2 \frac{D_{\max}}{\lambda_{\min}}}$). Thus ensuring the maximum sampled frequency is encompassed by the frequency grid, irrespective of n . Combining Equations 2.7 and 2.11, allows for solving for both n and d . This gives

$$n \geq \frac{1}{\epsilon} \frac{f_{\text{samp, max}}}{f_{\text{samp, min}}} + 1 = \frac{1}{\epsilon} \frac{\frac{D_{\max}}{\lambda_{\min}}}{\frac{D_{\min}}{\lambda_{\max}}} + 1, \quad (2.12)$$

and

$$d \leq \frac{\epsilon}{f_{\text{samp, max}} + \epsilon f_{\text{samp, min}}} = \frac{\epsilon}{\frac{D_{\max}}{\lambda_{\min}} + \epsilon \frac{D_{\min}}{\lambda_{\max}}}, \quad (2.13)$$

where n must be an integer and d can be a float. An alternative method to determine n and d , is to match d to the input image and calculate n from Equation 2.7. The value of d is then the spatial scale of the input image (in radians), divided by the number of pixels along the same axis. This method has the advantage that the reconstructed image has the same number of pixels along both axis as the input

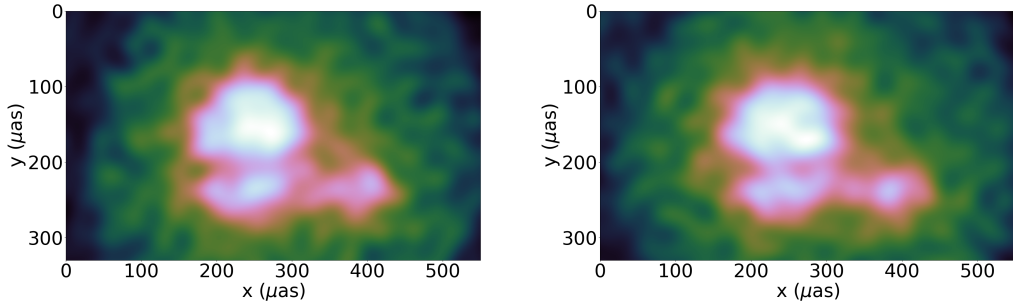


FIG. 2.15 – These Figures show the image reconstruction of Cyg X-1, see Figure 2.2 for the input image. The left Figure used the eIFT method and the right Figure used the IFFT method, with $\epsilon = 0.1$. Both used 10^5 source photons at a monochromatic energy of $E_{\text{phot}} = 6.4 \text{ keV}$, no background photons, no detector induced noise, a constant spacecraft roll of $5 \mu\text{rad}$ per simulator time step, 10 linearly spaced baselines from $D = 5 \text{ cm}$ to $D = 1 \text{ m}$, 5 slat-gap pairs, and all other XRI parameters adopted from [Willingale \(2004\)](#).

image. This allows for an image quality comparison method, which is discussed in Section 2.4.3. The disadvantage of this method is that it's only possible when an input image is given and known and can thus not be applied for image reconstruction using real observations.

It is important to recognise that the IFFT method is an approximation of the eIFT method, both for the mapping of the uv-coordinates to the frequency grid and in the calculations of the inverse Fourier transform. Figure 2.15 shows a comparison in image reconstruction for both the eIFT and IFFT methods, left and right panels respectively. No significant differences are visible between the two methods.

2.4.2 Periodogram

The current X-ray telescope with the smallest angular resolution is Chandra, with an angular resolution of $\theta_R \approx 0.5 \text{ as}$ ([Mori et al. 2001](#)). This is much larger than the maximum FoV of the XRI baselines, given by $\frac{\theta_b w}{D_{\min}}$ per slat-gap pair ([Uttley et al. 2020](#)). Given the XRI parameters used in Figure 2.15, the maximum FoV over all slat-gap pairs is $\sim 0.2 \text{ as}$. This does assume that all slat-gap pairs, of the baselines used for source finding / acquisition, are calibrated to a shared point on the detector per baseline. This comes at the cost of the SNR for observations, when compared

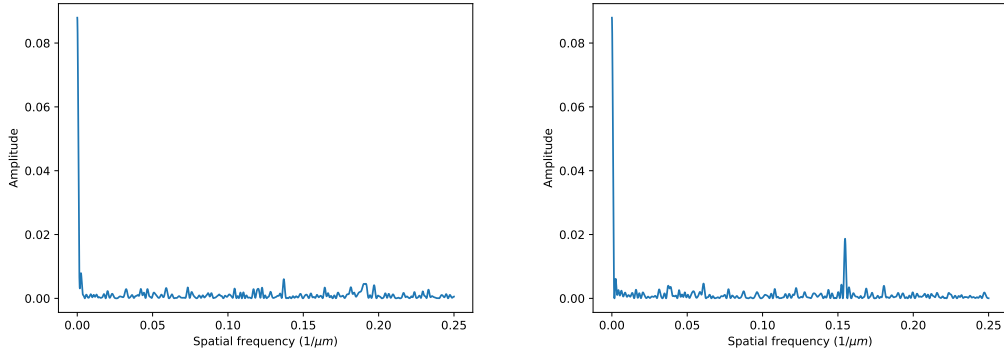


FIG. 2.16 – These Figures show the periodograms of Cyg X-1 (see Figure 2.2), with only background counts (left), and only source counts (right). The y-axes show P_k and the x-axes show the spatial frequencies (μm^{-1}). Both Figures use 10^2 total photons, with a monochromatic energy $E_{\text{phot}} = 6.4 \text{ keV}$, no detector induced noise, a constant spacecraft roll of 1 mrad per simulator time step, one XRI baseline of $D = 5 \text{ cm}$, 2 slat-gap pairs, and all other XRI parameters adopted from [Willingale \(2004\)](#). Both have their own and likely different random realisations. The set of photons for both are different and drawn from the same probability distributions separately.

to the case where each slat-gap pair, of the baselines used for observations, has its own calibrated point on the detector. The simulator assumes the former case, where all slat-gap pairs of a baseline have a shared point on the detector of the central fringe from an on-axis point source. Any astrophysical source that is not resolvable by Chandra, will appear as a point source in one of the pixels. These pixels are larger than to the largest FoV of the XRI baselines. Imaging the source requires to first find it inside of the pixel. For this, a search algorithm will need to be developed. The longer the search takes, the less observing time there is for the science cases. Any unresolved astrophysical source emits coherent photons, which result in the interference pattern discussed in Section 1.3.2, while background photons are incoherent and thus do not create an interference pattern. Finding a source therefore only requires detecting fringes. [Sriramanathan \(2024\)](#) made a pipeline for simulating incoming photons and performing fringe finding algorithms, based on theoretical significance equations derived by [Uttley \(2024\)](#). This pipeline has not yet been incorporated in the simulator. The fringe finding analysis is based on the power spectrum P_k of the detected photons, given by

$$P_k = |a_k|^2, \quad (2.14)$$

with a_k the discrete Fourier transform of the sample ([Uttley 2024](#)).

This module therefore has a new function, which calculates and displays the power spectrum as a periodogram. This is done by using the `Stingray` library in python, which can be used to generate power spectra for X-ray timing spectra ([Bachetti et al. 2023](#)). Interchanging the TOAs with the photon impact positions the desired periodogram is generated. It can also be used to determine the presence of fringes

when pushing the systems to their limits. This could be rapid spacecraft rotation, low source photon counts, high background counts, large path length perturbations, high detector noise, and many other relevant testing parameters. Figure 2.16 shows two periodograms of Cyg X-1 (see Figure 2.2), with only background counts (left), and only source counts (right). The peak of a perfect pure fringe pattern is at the inverse of the fringe spacing, $\frac{1}{\Delta y}$. In the periodogram with only background photons (left), there are no significant peaks visible. The right panel in Figure 2.16 shows a very clear and significant peak at $\sim 0.155 \mu\text{m}^{-1}$. Figure 2.17 shows the same periodogram, but having 10^2 source and background counts (2×10^2 total photon counts). Though the peak is lower, it is still detected at a significance of $\gtrsim 3\sigma$. This method of source detection only requires $\sim 10^2$ source counts compared to the 10^5 source counts used for the reconstructed images in Figure 2.15, and is able to clearly detect the source. Note that this analysis makes use of many idealizing assumptions, and is only meant as a proof of concept, as future work is needed for a detailed analysis.

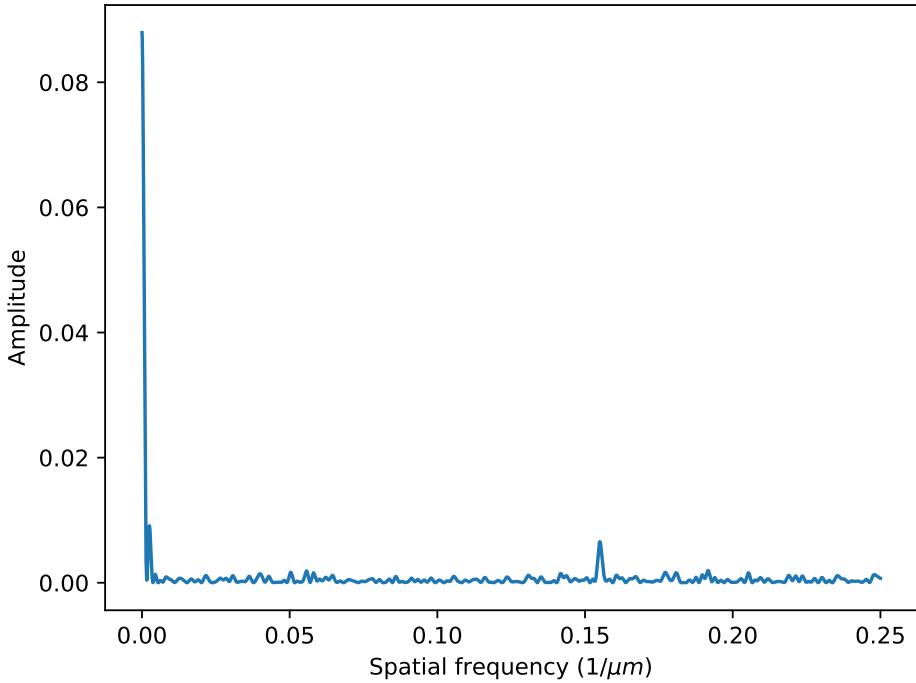


FIG. 2.17 – The Figure shows the periodogram of Cyg X-1 (see Figure 2.2), with both background and source counts. The y-axis shows P_k and the x-axis shows the spatial frequencies (μm^{-1}). The background and source counts both use 10^2 photons (10^4 total photons), both with a monochromatic energy $E_{\text{phot}} = 6.4 \text{ keV}$, no detector induced noise, a constant spacecraft roll of 1 mrad per simulator time step, one XRI baseline of $D = 5 \text{ cm}$, 2 slat-gap pairs, and all other XRI parameters adopted from [Willingale \(2004\)](#).

2.4.3 Image quality

For the analysis of possible science cases, it is best to have human qualitative assessment by experts in the respective fields. This process is too time intensive for large future XRI parameter space optimization. Therefore it is important to have a quantitative analyses of the reconstructed image quality, which can be used in optimization algorithms (e.g. gradient-based stochastic optimization methods, [Huan & Marzouk 2014](#)).

This module therefore has a new function, which quantifies the difference between the reconstructed and the input images. All other functions in the Analysis module directly analyse the deduced photon properties, where this function analyses the output of one of those functions. This makes it more of a post processing analysis function. To quantify the difference between the reconstructed and the input images, the sum of squared residuals (SSR) method is used. The SSR is calculated as

$$\text{SSR} = \sum_{ij} (R_{ij} - S_{ij})^2, \quad (2.15)$$

with R the reconstructed image, S the source image (i.e. input image), and i and j the pixels of each axis ([Heinemans 2020](#)). Therefore, this method can only be applied when the reconstructed and input images have the same number of pixels on both axis as one another. That is why the latter definition of d is chosen, as discussed in Section 2.4.1. Additionally, it is important to make the pixel values of both images comparable in scale. Such that when the reconstructed image matches all structures of the input image, the SSR value is 0. If not made comparable, the SSR value might indicate a poor quality image, even though it matches perfectly by eye. As the SSR looks at the absolute difference between pixel values. The applied normalization is given by

$$R_{ij, \text{norm}} = \frac{R_{ij} - R_{ij, \text{min}}}{R_{ij, \text{max}} - R_{ij, \text{min}}}, \quad (2.16)$$

with $R_{ij, \text{norm}}$ the normalized pixel values, $R_{ij, \text{min}}$ the minimum pixel value, and $R_{ij, \text{max}}$ the maximum pixel value of the reconstructed image R . The same equation is applied to the input source image pixels S_{ij} . An example of the use of the SSR method as a quantity to judge the reconstructed image quality is discussed in Section 3.3 and shown in Figure 3.3. The effects of the choice of normalization method is discussed in Section 4.1.

Chapter 3

Results

The main goal of this thesis is to fix (see Section 2.3.3), improve (see Section 2.4.1), and to add (see all other Sections in Chapter 2) to the simulator made by [van Hese \(2023\)](#). A goal for the overall project of the proposed space mission is to use the simulator for investigating and defining science cases and to optimise and set requirements for the development of the instrumentation of and the spacecraft as a whole (see [Uttley et al. 2020](#)). This chapter serves to show and discuss results, which serve the latter goal. As the main focus is on the development of the simulator, the results are a subset of what is possible to obtain from the simulator.

3.1 Speed comparison exact inverse Fourier transform and inverse fast Fourier transform

Section 2.4.1 discussed the eIFT and the IFFT reconstruction methods. Figure 3.1 shows the reconstruction time (s) as a function of the number of source photons for different input source image models and for these methods. In most cases the IFFT method is faster. The only exception being the Sgr A* model at 10^3 source photons. The eIFT method appears to show a linear increase in a log-log graph, suggesting a power function like relation between the reconstruction time and the number of photons, i.e.

$$t_{\text{recon}} \propto N_{\text{phot}}^b, \quad (3.1)$$

with t_{recon} the reconstruction time (s), N_{phot} the number of source photons, and b the corresponding exponent (based on the slope in the log-log graph). Based on the data in Appendix B, $b \approx 1$. While the IFFT method remains effectively flat as a function of N_{phot} for all input models up to $N_{\text{phot}} \approx 10^5$. This is expected, as the timing of

the IFFT method depends on n , which is independent of N_{phot} (see Equations 2.7 and 2.12). Due to the choice of d and using Equation 2.7 for n , n depends on the number of pixels along the largest axis of the input image and the chosen value of ϵ . The difference in the number of pixels along the largest axis is the main driver of the difference in timings between the different input models, for the IFFT method. The difference in timings between the different input models for the eIFT method is mainly driven by the total number of pixels in the input image. The Sgr A* input model has more pixels along its largest axis, but less total number of pixels compared to the AU Mic input model. That is why the Sgr A* model is faster in the eIFT method and slower in the IFFT method, compared to the AU Mic model. The Cyg X-1 input model shows a significant increase in t_{recon} above $N_{\text{phot}} \approx 10^5$. The reconstruction consists roughly of two phases. The first calculates the uv-coordinates and corresponding Fourier components of each photon. This happens in both the eIFT and the IFFT methods. The second part is the inverse Fourier transform, which is different for the two reconstruction methods. The reason for the significant increase in t_{recon} above $N_{\text{phot}} \approx 10^5$ for the Cyg X-1 model is that the computational time of the first part begins to and ends up completely dominating t_{recon} . This first part is dependent on N_{phot} . The same is also true for the AU Mic model at $N_{\text{phot}} \approx 10^7$, with this increase being clear from the data used (See Table B.2) and not as clear in Figure 3.1. The eIFT method simulations were performed up to $N_{\text{phot}} \approx 10^5$ due to time restrictions.

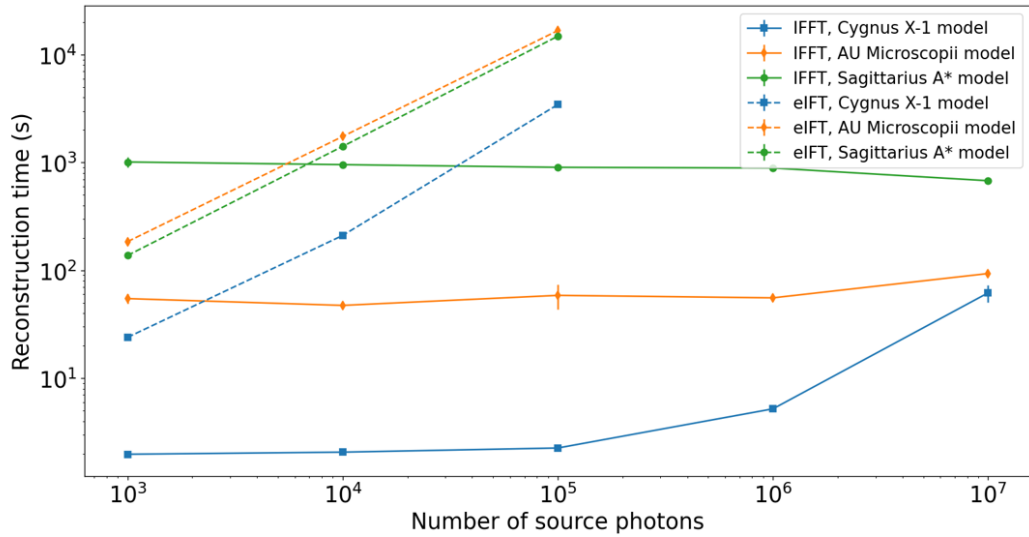


FIG. 3.1 – This Figure shows the reconstruction time (s) as a function of the number of source photons for different input source image models and for the eIFT and the IFFT reconstruction methods. The dashed and solid lines represent the eIFT and IFFT model timings, respectively. The blue lines with square markers represent the Cyg X-1 input source model. The orange lines with diamond markers represent the AU Mic input source model. The green lines with circle markers represent the Sgr A* input source model. The markers represent the means of three simulations, with their respective error bars being the standard deviations over those simulations. All data points used only source photons at a monochromatic energy of $E_{\text{phot}} = 6.4 \text{ keV}$, no background photons, no detector induced noise, a constant spacecraft roll of 0.5 mrad per simulator time step, 10 linearly spaced baselines from $D = 5 \text{ cm}$ to $D = 1 \text{ m}$, and all other XRI parameters adopted from [Willingale \(2004\)](#). The IFFT model uses $\epsilon = 0.1$. For all data used in this Figure, see Appendix B.

3.2 Background effects

Section 2.1.2 discussed the implementation of a uniform X-ray background on an input image model. In Figure 3.2 the effects of background is shown. The left Figure shows the reconstructed image based only on 10^6 source photons ($E_{\text{phot}} = 6.4 \text{ keV}$). The right Figure has the same source photons and a uniform X-ray background of 10^6 monochromatic ($E_{\text{phot}} = 6.4 \text{ keV}$) photons, thus using equal (amounts) photons for the background. This clearly worsens the quality of the reconstructed image, though blurring. Yet not to the extent that all information is lost. On the contrary, the reconstructed image is still clear enough to recognize and study many details of the Cyg X-1 system (see Figure 2.2 for the input model image). This is expected, as the source photons are correlated and the background photons are not. The background photons thus only lower the SNR without distorting the information encoded within the full fringe and diffraction pattern (for the full pattern description, see Section 1.3.2). For Figure 3.2, the XRI parameters are mostly adopted from Willingale (2004), with $N_{\text{pairs}} = 30$ per baseline. Using many slat-gap pairs increases S in Equation 2.1 and thus also increases A_{Eff} . This results in detecting more photons, faster. Having many slat-gap pairs also spreads out those photons more, lowering their amplitudes. This increases the sensitivity to, background or otherwise induced, reduction of the SNR. Note that Figure 3.2 shows the effect that an X-ray background has on the reconstructed image and is not a thorough analysis to investigate engineering requirements with respect to the allowed maximum background. Though the latter is possible with the simulator.

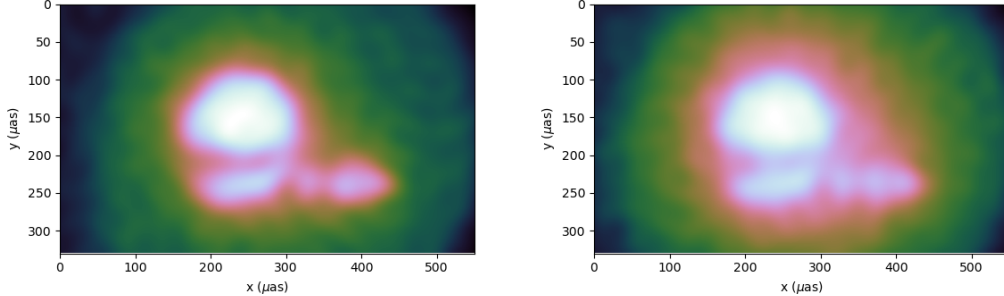


FIG. 3.2 – These Figures show the image reconstruction of Cyg X-1, see Figure 2.2 for the input image. The left Figure used only source photons, while the right Figure has an additional 10^6 monochromatic ($E_{\text{phot}} = 6.4 \text{ keV}$) background photons. Both Figures used the IFFT reconstruction method ($\epsilon = 0.1$), 10^6 source photons at a monochromatic energy of $E_{\text{phot}} = 6.4 \text{ keV}$, no detector induced noise, a constant spacecraft roll of 0.5 mrad per simulator time step, 10 linearly spaced baselines from $D = 5 \text{ cm}$ to $D = 1 \text{ m}$, and all other XRI parameters adopted from [Willingale \(2004\)](#).

3.3 Reconstructed image quality: number of photons

Observing time on space telescopes is often in high demand, resulting in every second being valuable. Therefore it is important to know beforehand what minimum integration time (i.e. observing time) is needed to get a reconstructed image of sufficient quality to perform the desired science. The required integration time follows from the source spectrum ($N(E)$) and the instrument effective area ($A_{\text{Eff}}(E)$). As the integration time is N_{phot} divided by Equation 2.3. To this end, Figure 3.3 shows the SSR (as discussed in Section 2.4.3) as a function of the number of source photons for the Cyg X-1 input model. The SSR values show an asymptotic decay as a function of N_{phot} . Additionally, the respective errors also appear to asymptotically decrease as a function of N_{phot} . The smaller the SSR values, the better the reconstructed image quality. The SSR values are not expected to reach 0, as $\theta_{R, \text{max}}$, from D_{max} and $E_{\text{phot}, \text{max}}$, is larger than the input image angular size. There will thus be structures in the input image which cannot be reconstructed given D_{max} and $E_{\text{phot}, \text{max}}$. Section 4.1 will further discuss the SSR method, as a measure for reconstructed image quality.

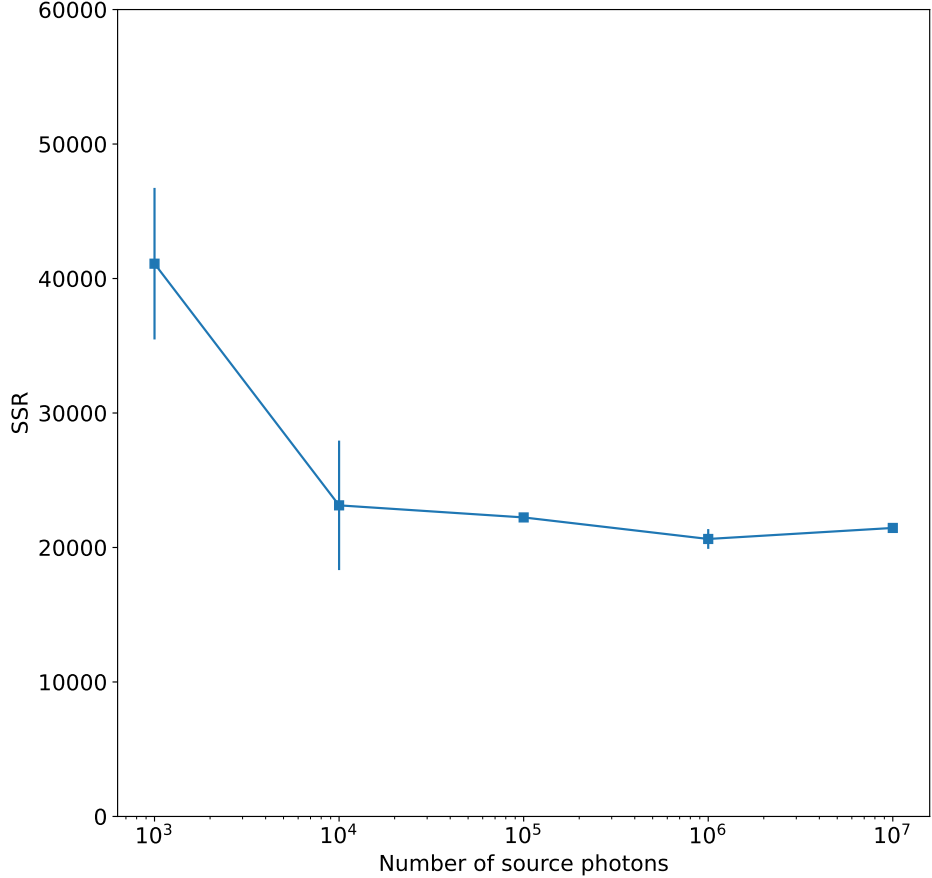


FIG. 3.3 – This Figure shows the SSR (as discussed in Section 2.4.3) as a function of the number of source photons for the Cyg X-1 input model. The markers represent the means of three simulations, with their respective error bars being the standard deviations over those simulations. The reconstructed images used for all data points used the IFFT reconstruction method ($\epsilon = 0.1$), source photons at a monochromatic energy of $E_{\text{phot}} = 6.4 \text{ keV}$, no detector induced noise, no background photons, a constant spacecraft roll of 0.5 mrad per simulator time step, 10 linearly spaced baselines from $D = 5 \text{ cm}$ to $D = 1 \text{ m}$, and all other XRI parameters adopted from [Willingale \(2004\)](#). See Appendix C for all reconstructed images, their respective residuals, and corresponding SSR values used for this Figure.

Chapter 4

Discussion

4.1 Sum of squared residuals accuracy

As discussed in Section 2.4.3, the SSR method is adopted from Heinemans (2020). They discuss structural shifts of the reconstructed image, where they assume a linear shift such that when there is no noise

$$R_{ij} = A + B \times S_{ij}, \quad (4.1)$$

with A and B parameters used to minimize the SSR, and additional noise is expected. The SSR is given by

$$\text{SSR} = \sum_{ij} (R_{ij} - (A + B \times S_{ij}))^2. \quad (4.2)$$

Despite this, the SSR values they report are either on the order of 10^9 or 10^7 . While testing different normalization methods for Figure 3.3, it became apparent that they all result in roughly the same trend in SSR values as a function of N_{phot} . While the absolute SSR values changed. The choice of normalization thus effects the relative change in the SSR values and those effect the relevance of the change. If the absolute change is always 1, then while the absolute value is 1000 it is considered an insignificant change, but with an absolute value of 2 it would be considered a very significant improvement. Figure 4.1 shows the residual of the reconstructed image (see the left Figure in Figure 3.2) compared to the input image (see Figure 2.2). Neither image is normalised before calculating the residual and corresponding SSR value ($\sim 1.2 \times 10^9$). Besides the very large SSR value, the residual also looks bad. The differences appear to be zero around the source and very low on the source. As if the reconstructed image is zero everywhere. Which is clearly not the case when looking at left Figure in Figure 3.2. No normalisation results in very high SSR values and a poor representation of the reconstructed image quality. Figure 4.2 shows the same residual plot, but with both

reconstructed and input images normalised to have a mean of one. This successfully brings down the SSR value to $\sim 9.2 \times 10^5$. This normalisation method still faces the same issue of the residual not being representative of the reconstructed image quality due to the same reasons. Figure 4.3 shows the same residual plot, but with both reconstructed and input images normalised to have a sum of one (resulting in a probability distribution). This successfully brings down the SSR value even further to $\sim 2.8 \times 10^{-5}$. However, this normalisation method still faces the same issue of the residual not being representative of the reconstructed image quality due to the same reasons. Figure 4.4 shows the same residual plot, but with both reconstructed and input images normalised using $R_{ij, \text{norm}} = \frac{R_{ij} - R_{ij, \text{min}}}{R_{ij, \text{max}}}$, before calculating the residual and corresponding SSR value ($\sim 2.2 \times 10^4$). The SSR value is large but manageable. Much more importantly, the residual now represents the visual reconstructed image quality. The difference in pixel values is zero in the centre of the large bright region and towards the edges. The blurriness of limited $\theta_{R, \text{min}}$ is also visible, with the difference increasing towards the source edges. The problem with this normalization is that if $R_{ij} = kS_{ij} + c$, with k and c constants, $R_{ij, \text{norm}} \neq S_{ij, \text{norm}}$, thus requiring the normalization according to Equation 2.16. Figure 4.5 shows the same residual plot, but with both reconstructed and input images normalised according to Equation 2.16 and corresponding SSR value ($\sim 2.1 \times 10^4$). This has the same advantages as the residual in Figure 4.4, with the important difference of $R_{ij, \text{norm}} = S_{ij, \text{norm}}$, if $R_{ij} = kS_{ij} + c$.

This last normalisation method still has limitations. Based on the reconstructed images and corresponding residuals shown in Appendix C, there is still a change visible by eye from 10^5 to 10^6 source photons. This does not, however, translate in to a meaningful change in the SSR value. It might thus be that the SSR method is not the correct method for quantifying the reconstructed image quality. As there are no clear outliers, nor structural source location shifts, which could dominate the SSR values and thereby drown out this improvement. Alternatively, it might be that a different normalization is required, as it has a strong effect on the SSR value. Otherwise, the observed SSR behaviour might be the result of an undiscovered bug in the simulator.

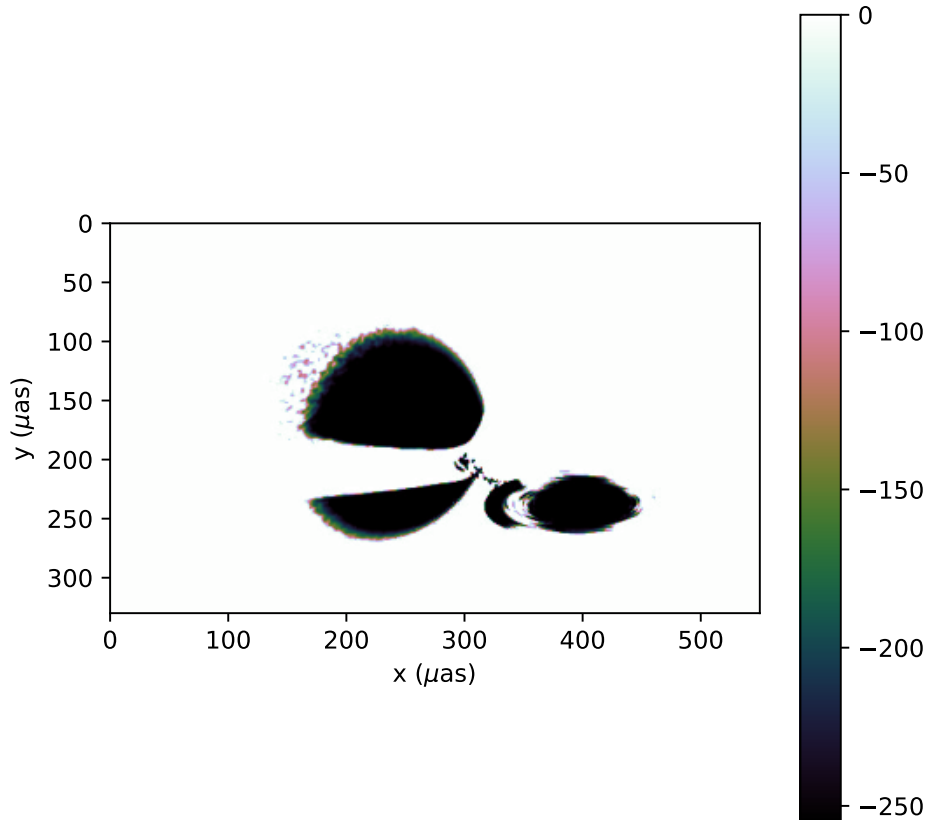


FIG. 4.1 – This Figure shows the residual of the reconstructed image (see the left Figure in Figure 3.2) compared to the input image (see Figure 2.2). Neither image is normalised before calculating the residual and corresponding SSR value (1236046331.8068929). The image reconstruction used the IFFT reconstruction method ($\epsilon = 0.1$), 10^6 source photons at a monochromatic energy of $E_{\text{phot}} = 6.4 \text{ keV}$, no detector induced noise, no background photons, a constant spacecraft roll of 0.5 mrad per simulator time step, 10 linearly spaced baselines from $D = 5 \text{ cm}$ to $D = 1 \text{ m}$, and all other XRI parameters adopted from [Willingale \(2004\)](#).

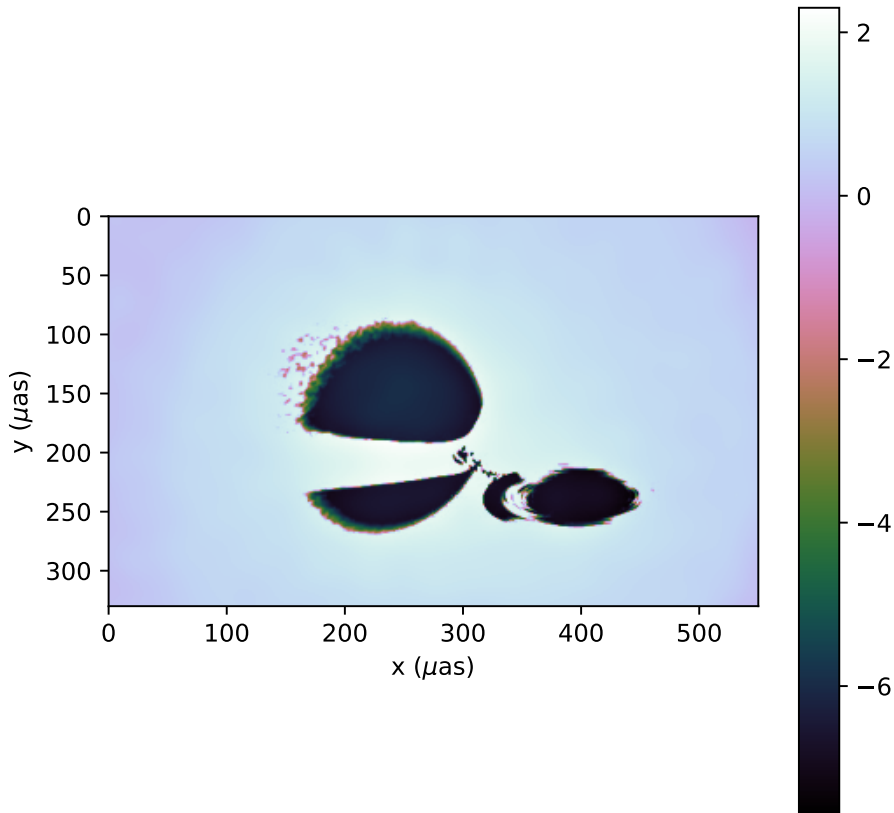


FIG. 4.2 – This Figure shows the residual of the reconstructed image (see the left Figure in Figure 3.2) compared to the input image (see Figure 2.2). Both images are normalised by dividing them by the mean of their own pixel values before calculating the residual and corresponding SSR value (923169.8666040525). The image reconstruction used the IFFT reconstruction method ($\epsilon = 0.1$), 10^6 source photons at a monochromatic energy of $E_{\text{phot}} = 6.4 \text{ keV}$, no detector induced noise, no background photons, a constant spacecraft roll of 0.5 mrad per simulator time step, 10 linearly spaced baselines from $D = 5 \text{ cm}$ to $D = 1 \text{ m}$, and all other XRI parameters adopted from [Willingale \(2004\)](#).

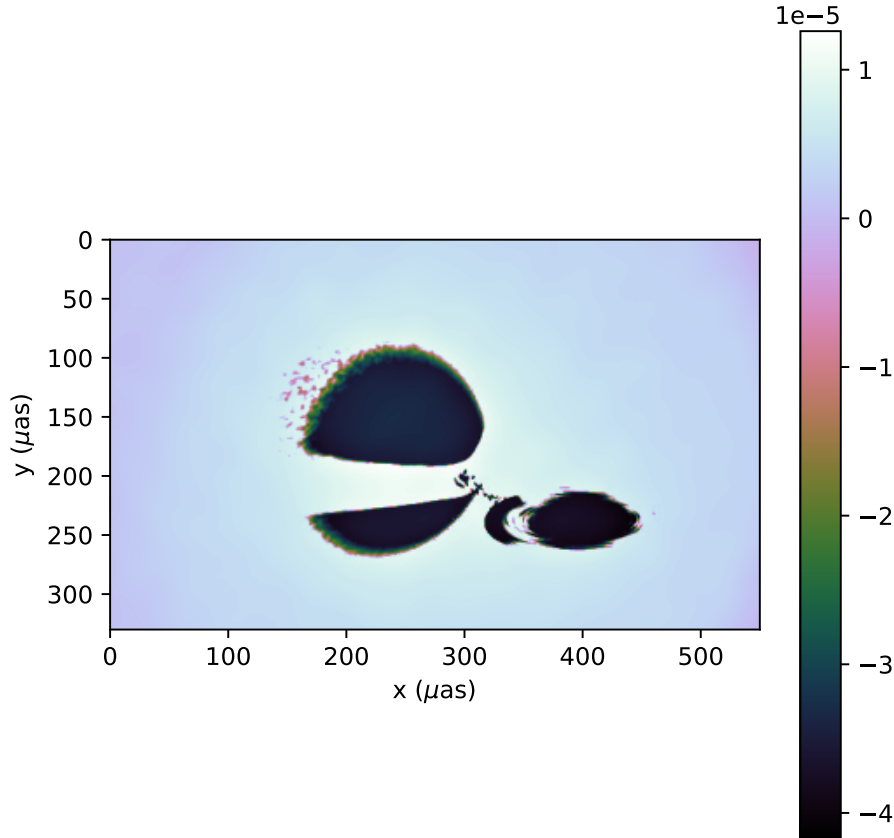


FIG. 4.3 – This Figure shows the residual of the reconstructed image (see the left Figure in Figure 3.2) compared to the input image (see Figure 2.2). Both images are normalised by dividing them by the sum of their own pixel values before calculating the residual and corresponding SSR value ($2.7978997310576186 \times 10^{-5}$). The image reconstruction used the IFFT reconstruction method ($\epsilon = 0.1$), 10^6 source photons at a monochromatic energy of $E_{\text{phot}} = 6.4 \text{ keV}$, no detector induced noise, no background photons, a constant spacecraft roll of 0.5 mrad per simulator time step, 10 linearly spaced baselines from $D = 5 \text{ cm}$ to $D = 1 \text{ m}$, and all other XRI parameters adopted from [Willingale \(2004\)](#).

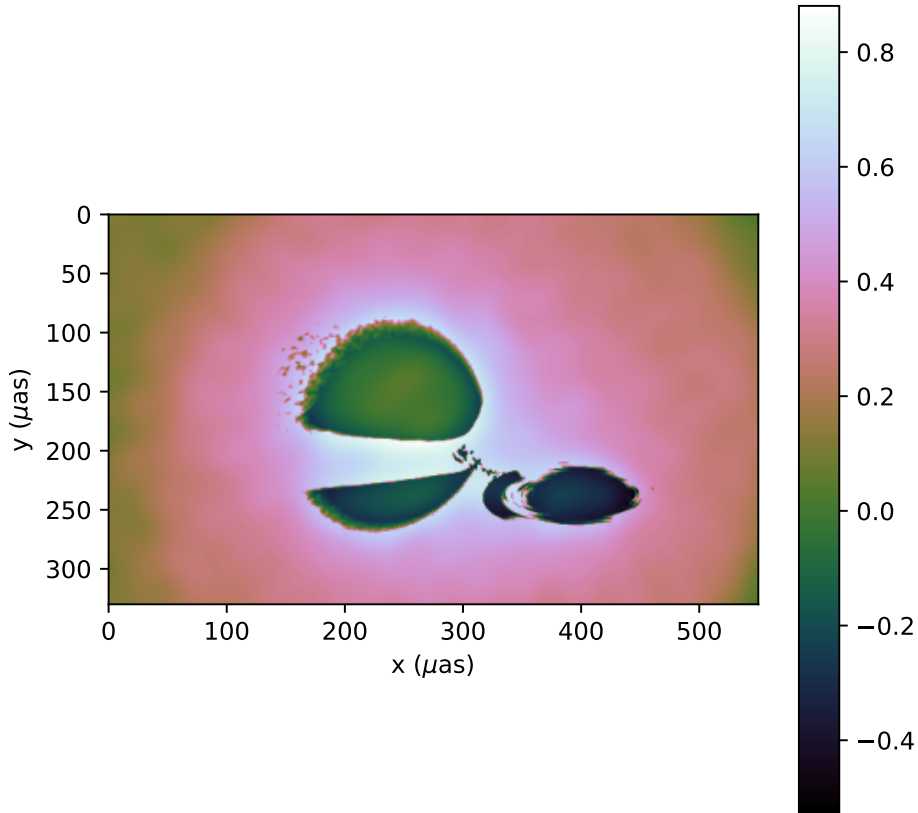


FIG. 4.4 – This Figure shows the residual of the reconstructed image (see the left Figure in Figure 3.2) compared to the input image (see Figure 2.2). Both images are normalised using $R_{ij, \text{norm}} = \frac{R_{ij} - R_{ij, \text{min}}}{R_{ij, \text{max}}}$, before calculating the residual and corresponding SSR value (22273.718713430975). The image reconstruction used the IFFT reconstruction method ($\epsilon = 0.1$), 10^6 source photons at a monochromatic energy of $E_{\text{phot}} = 6.4 \text{ keV}$, no detector induced noise, no background photons, a constant spacecraft roll of 0.5 mrad per simulator time step, 10 linearly spaced baselines from $D = 5 \text{ cm}$ to $D = 1 \text{ m}$, and all other XRI parameters adopted from [Willingale \(2004\)](#).

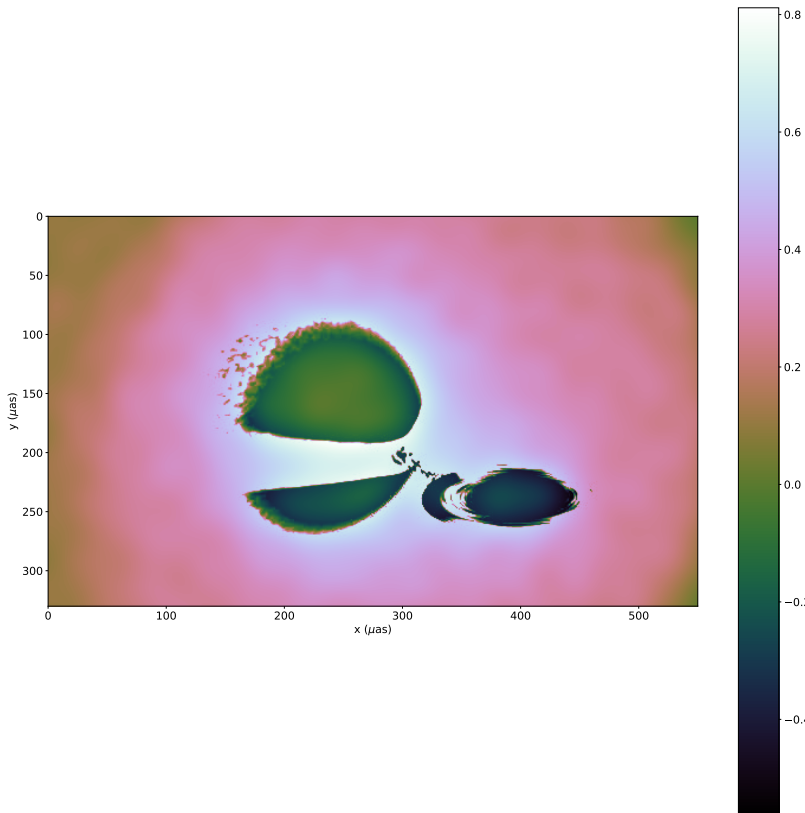


FIG. 4.5 – This Figure shows the residual of the reconstructed image (see the left Figure in Figure 3.2) compared to the input image (see Figure 2.2). Both images are normalised using Equation 2.16 before calculating the residual and corresponding SSR value (21054.562980625054). The image reconstruction used the IFFT reconstruction method ($\epsilon = 0.1$), 10^6 source photons at a monochromatic energy of $E_{\text{phot}} = 6.4 \text{ keV}$, no detector induced noise, no background photons, a constant spacecraft roll of 0.5 mrad per simulator time step, 10 linearly spaced baselines from $D = 5 \text{ cm}$ to $D = 1 \text{ m}$, and all other XRI parameters adopted from [Willingale \(2004\)](#).

4.2 Future work

Much work has already gone into making a functioning simulator, making it more efficient and more accurate / realistic. At the same time, there is still much more to add and improve. Additionally, there is still a lot of information that can be extracted using the simulator, which would inform the science cases, scientific requirements, and regions of interest for technology development. In this chapter some of the possible future work is discussed in no particular order.

4.2.1 Input data

The example input sources have been discussed in Section 2.1 and in [van Hese \(2023\)](#). Input source model images are limited to a single spectrum over the entire source. As the input is a two dimensional image, with the relative pixel values representing their relative brightness, and an additional input possibility for the overall spectrum of the source. In the future this could be expanded to accept data cubes, containing spectral information of each pixel. This would allow the output from separate simulations of astrophysical sources to be directly used as input for the XRIimulator. Additionally, it could be expanded to also accept time variable input sources, as would be important for modeling the expected reconstructed images for sources which change on timescales relevant with respect to the required integration time. Alternatively, the input could be expanded to accept pre-sampled photons. Where the user has a separate simulation of a source, which samples photons as they would reach the spacecraft. Or one step further, direct photon events from a detector may be supplied, where the XRIimulator is used for the analysis tools provided (see Section 2.4).

4.2.2 Background function

The current implementation of background X-rays is discussed in Section 2.1.2. Though a background spectrum can already be given, it is not yet sampled. This would be the first addition to the background implementation. Additionally, the background can be made more realistic. For this purpose, it would be best to put the background sampling in a separate function inside of the Image module. This would increase the ease and clarity of the background implementation. Different types of background could be included. These may include, but are not limited to, uniform background (currently the only implemented type, see Section 2.1.2), uniform background excluding the source emission regions, additional X-ray source in the FoV of (some of) the baselines, stray light models, and others.

4.2.3 Cosmic rays

Another significant source of non-source photon detections are cosmic rays. They have been given their own subsection due to their drastically different effect on the detector output. Cosmic rays do not behave like simple incoherent background photons. A single cosmic rays can saturate multiple detector pixels. If a source photon was already absorbed in one of these affected pixels, but not yet read out by the detector, its information is lost. This assumes the cosmic ray was identified and all affected pixels were read out, without saving their outputs. When the cosmic ray is not identified, it can result in very wrong deduced photon properties. Implementation of cosmic rays requires an additional detector parameter for the read out frequency, sampling cosmic rays, modeling their resulting deduced photon properties, and potentially cosmic ray detection algorithms with correction algorithms. Cosmic ray detection and correction algorithms already exist ([van Dokkum et al. 2012](#)), and could be adapted into the XRIimulator pipeline.

4.2.4 More realistic detector

As previously discussed (Section 4.2.3), in order to perform more detailed performance studies on the proposed space mission, a more detailed and realistic detector class is required. The new detector class, discussed in Section 2.2.3, contains mainly legacy and basic functionalities ([van Hese 2023](#)). A big step towards a more realistic detector would be the addition and implementation of an instrument response matrix. This can be simulated and saved outside of the XRIimulator and put in as a text-like file. The instrument response matrix maps the real incoming photon energies to a detector channel, which are calibrated to specific central energies and energy widths. The instrument response matrix also encodes the detector A_{Eff} . Another additional input would be the detector readout frequency. Potentially also including the energy usage of the detector as a function of its readout frequency and the pre-processing of the detector output to deduced photon properties, with or without cosmic ray corrections. This would help inform the amount of cosmic ray shielding that is required and check if the detector energy consumption fits within the available energy envelope. Shielding adds mass, which has to remain within the maximum mass (see Figure 1.2) and cosmic ray correction contributes a significant amount of the detector energy consumption for NewAthena ([Manhart & Meidinger 2018](#); [Meidinger et al. 2018](#)).

4.2.5 Path length perturbation sources

As discussed in Section 2.2.2, a function is implemented to apply path length perturbations as a function of time. The actual sources for these are not yet implemented. These include, but are not limited to, thermal fluctuations, vibrations, stress induced deformations, deposits forming on optical surfaces, and more. These could either all be simulated separately and whose output path length differences as a function of time are imported as a text-like file. Which is then read and interpolated by the existing function. Alternatively, some low computationally intensive perturbations could be included in and modeled by the XRIimulator.

4.2.6 Spacecraft wobble correction

As discussed in Section 2.2, a preliminary implementation of spacecraft wobble is already implemented. The final spacecraft will have ring-laser gyroscopes, which can measure the spacecraft wobble (see Section 2.2). The spacecraft wobble will translate into an observed shift in θ , compared to the original or zero pointing. The knowledge of the spacecraft pointing and rotation from the ring-laser gyroscopes can be used to calculate the expected fringe shift. In theory, this can then correct the wobble induced fringe shift and diminish its effects on the reconstructed image. This will require the implementation of both the ring-laser gyroscopes and a wobble correction algorithm.

4.2.7 More testing

The tests performed in Chapter 3 are by no means exhaustive. This thesis focuses on the simulator code itself and the information that can be extracted is a nice proof of concept. Many more tests can be performed to extract even more information. These can include, but are not limited to, investigating image quality as a function of energy noise, positional noise, spacecraft wobble, spacecraft rotation, and more. These would help inform possible science cases and engineering requirements of the spacecraft.

4.2.8 User manual

All modules described in Chapter 2 are well documented and commented, allowing for people unfamiliar with the code to quickly understand its workings. A detailed

manual would allow for the same to be true for executing all the modules to execute the entire simulator, similar to X-PSI (<https://xpsi-group.github.io/xpsi/index.html>, Riley et al. 2023). A detailed walk through of all capabilities and drawbacks will save time in getting up to speed with the code and allow for more time using it to extract information from, or improve, the simulator. The manual could also include common errors, mistakes, and weird outputs. This, again, reduces time spent on understanding what is going wrong, by showing quick fixes to the problems.

Chapter 5

Conclusion

In astronomy, X-rays are very useful for probing multiple different systems and physics. This is due to the fact that X-rays can be produced in significant amounts by atomic, thermal and non-thermal processes. Telescopes have, in most wavelength bands, reached the theoretical diffraction limit on angular resolution. A major exception being the X-ray bands. This is due to the difficulty of manufacturing focusing optics for X-rays to a precision of a fraction of the wavelength. X-ray interferometry may hold the key to overcoming the challenges and achieving angular resolutions closer to the theoretical limit. An end-to-end simulator of the proposed spacecraft using X-ray interferometry is a very important tool in the current development stage. It can show scientists what is possible within mechanical limitations and inform engineers about the required tolerances. This thesis focuses on the corrections, improvements and expansions of the simulator.

The simulator is sped up, with an image reconstruction method, which is mostly independent of the number of photons. This has allowed for an X-ray background and spectral information to be added. The effect of background is shown to be manageable. The reconstructed image is blurred, due to a decreasing signal to noise ratio, but retaining the useful information in visible structures. The quality of the reconstructed images can be quantified using the sum of squared residuals method. Though the normalization used in this method can still be further refined, it was used to show the improvement that the number of source photons has on the reconstructed image quality. Many more tests can be performed in future works to extract more information from the simulator. Additionally, more physics and features can be incorporated to further refine the potential science cases and spacecraft requirements.

Appendix A

Iridium reflectivity

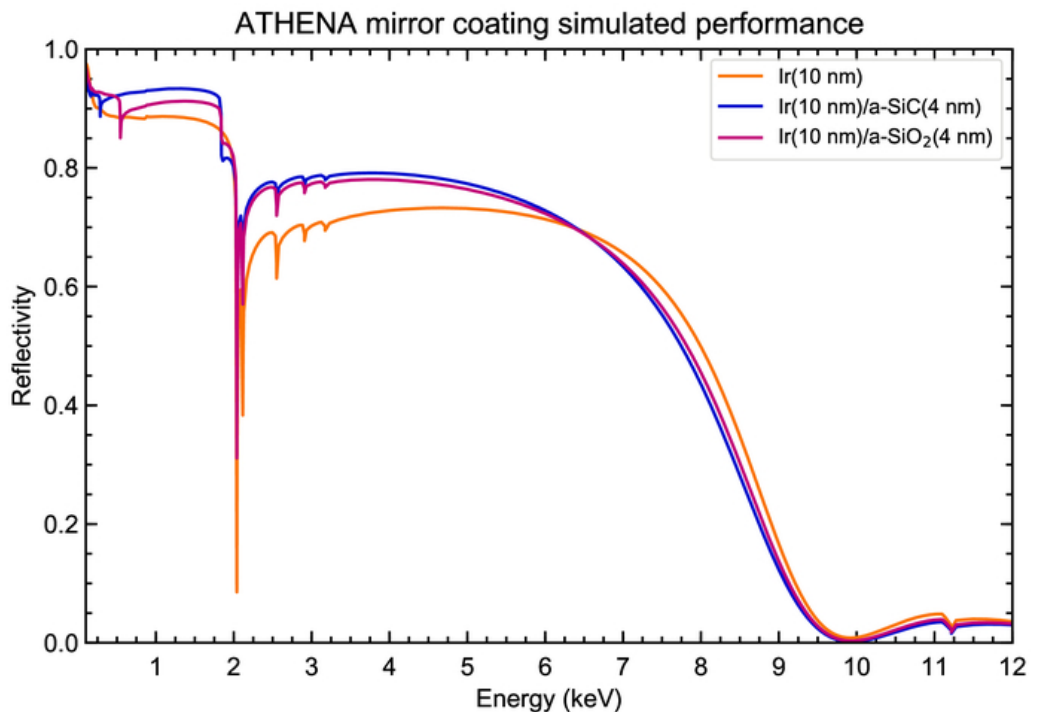


FIG. A.1 – Simulated 0.1-12 keV performance of Ir, Ir/SiC and Ir/SiO₂ coatings at a fixed grazing incidence angle of 0.6 deg. Average root-mean-square (RMS) roughnesses of 0.45 nm are assumed in each case. Adopted from [Svendsen et al. \(2019\)](#).

Appendix B

Timing data tables

Cyg X-1 input model				
Method	Counts	1	2	3
eIFT	10^3	23.580647706985474 s	25.362747192382812 s	22.795028924942017 s
	10^4	210.63913583755493 s	210.20079231262207 s	210.90441608428955 s
	10^5	3434.2364015579224 s	3433.2942633628845 s	3471.781613588333 s
IFFT	10^3	1.9631474018096924 s	1.964709758758545 s	1.9854674339294434 s
	10^4	2.2012534141540527 s	1.966874361038208 s	2.0153300762176514 s
	10^5	2.2482523918151855 s	2.269254446029663 s	2.236830949783325 s
	10^6	5.281658172607422 s	5.194562196731567 s	5.110870122909546 s
	10^7	76.57766318321228 s	60.02653241157532 s	48.7470543384552 s

TABLE B.1 This table has all the data used to calculate the data points for the blue lines with square markers in Figure 3.1, the Cyg X-1 input model. For both the dashed and solid lines, the eIFT and IFFT methods respectively.

AU Mic input model				
Method	Counts	1	2	3
eIFT	10^3	183.58709502220154 s	196.87431049346924 s	173.3073971271515 s
	10^4	1749.9228456020355 s	1753.175392627716 s	1728.207153081894 s
	10^5	18495.82885479927 s	15852.687741041183 s	15807.301728248596 s
IFFT	10^3	60.394174098968506 s	56.220364570617676 s	47.45090055465698 s
	10^4	47.061010122299194 s	46.749977111816406 s	48.105910778045654 s
	10^5	45.7546546459198 s	50.226318359375 s	79.85661053657532 s
	10^6	55.69122290611267 s	59.75592279434204 s	51.28024196624756 s
	10^7	89.45436525344849 s	90.06537652015686 s	100.69448661804199 s

TABLE B.2 This table has all the data used to calculate the data points for the orange lines with diamond markers in Figure 3.1, the AU Mic input model. For both the dashed and solid lines, the eIFT and IFFT methods respectively.

Sgr A* input model				
Method	Counts	1	2	3
eIFT	10^3	138.07716751098633 s	136.75148916244507 s	137.3305847644806 s
	10^4	1435.3916058540344 s	1389.2145638465881 s	1408.7995910644531 s
	10^5	14898.095885276794 s	14824.884345769882 s	14773.56988620758 s
IFFT	10^3	1144.2079203128815 s	996.4088551998138 s	891.9247572422028 s
	10^4	1007.846200466156 s	917.9999792575836 s	940.4920704364777 s
	10^5	874.2314040660858 s	942.5474908351898 s	889.7235646247864 s
	10^6	907.2256791591644 s	878.0419678688049 s	880.2273998260498 s
	10^7	701.7326200008392 s	668.9526920318604 s	662.4195463657379 s

TABLE B.3 This table has all the data used to calculate the data points for the green lines with circle markers in Figure 3.1, the Sgr A* input model. For both the dashed and solid lines, the eIFT and IFFT methods respectively.

Appendix C

Reconstructed images, their respective residuals, and sum of squared residuals values

Counts	1	2	3
10^3	42828.458816524726	33503.36914274371	46978.78301213146
10^4	28969.68194029493	23250.476151652685	17179.89022678827
10^5	21933.580314071376	22592.45299844117	22179.022891041142
10^6	21042.891867355058	21256.150203939804	19600.885579116533
10^7	21272.28941244448	21365.088373019546	21722.79599986528

TABLE C.1 This table has all the SSR values used to calculate the data points in Figure 3.3.

Appendix C. Reconstructed images, their respective residuals, and sum of squared residuals values

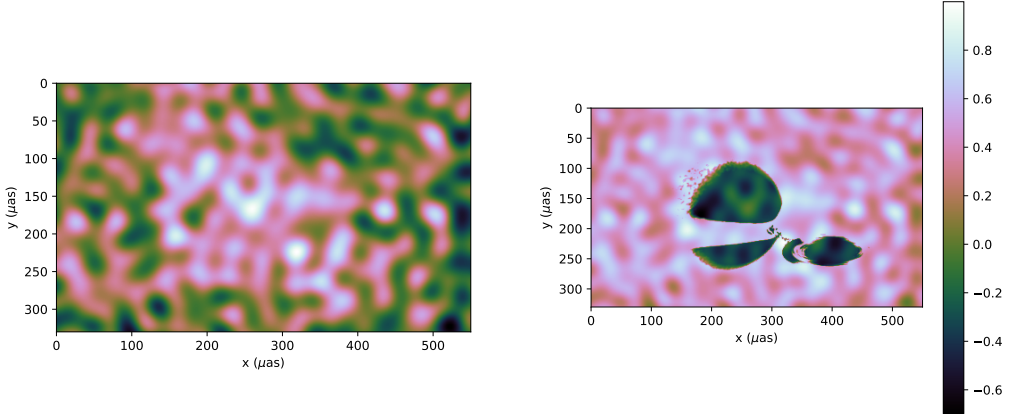


FIG. C.1 – These Figures show the reconstructed image (left) and its residual compared to Figure 2.2 (right), run 1. The image reconstruction used the IFFT reconstruction method ($\epsilon = 0.1$), 10^3 source photons at a monochromatic energy of $E_{\text{phot}} = 6.4 \text{ keV}$, no detector induced noise, no background photons, a constant spacecraft roll of 0.5 mrad per simulator time step, 10 linearly spaced baselines from $D = 5 \text{ cm}$ to $D = 1 \text{ m}$, and all other XRI parameters adopted from [Willingale \(2004\)](#).

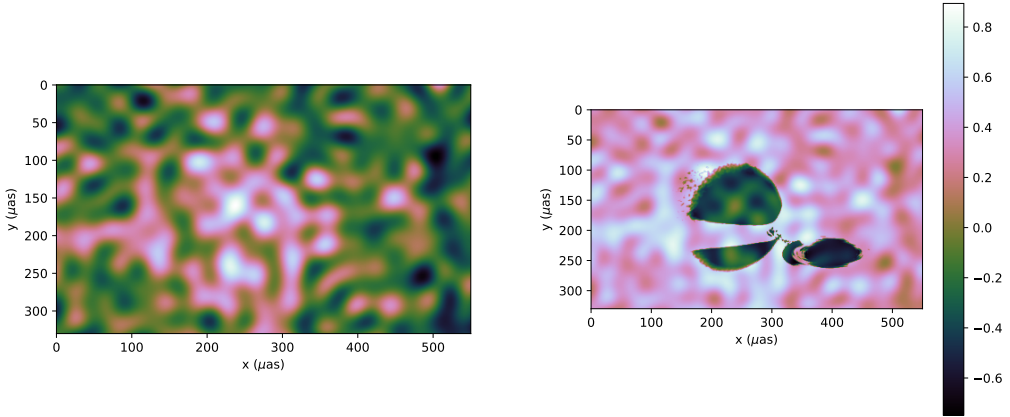


FIG. C.2 – These Figures show the reconstructed image (left) and its residual compared to Figure 2.2 (right), run 2. The image reconstruction used the IFFT reconstruction method ($\epsilon = 0.1$), 10^3 source photons at a monochromatic energy of $E_{\text{phot}} = 6.4 \text{ keV}$, no detector induced noise, no background photons, a constant spacecraft roll of 0.5 mrad per simulator time step, 10 linearly spaced baselines from $D = 5 \text{ cm}$ to $D = 1 \text{ m}$, and all other XRI parameters adopted from [Willingale \(2004\)](#).

Appendix C. Reconstructed images, their respective residuals, and sum of squared residuals values

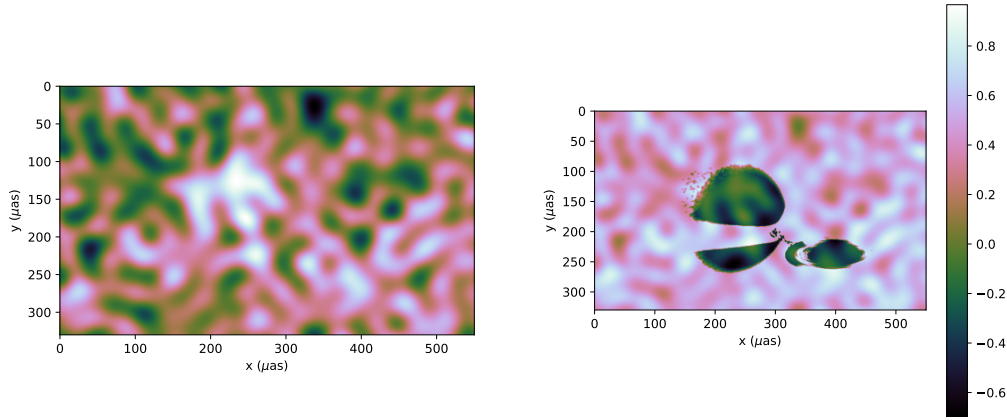


FIG. C.3 – These Figures show the reconstructed image (left) and its residual compared to Figure 2.2 (right), run 3. The image reconstruction used the IFFT reconstruction method ($\epsilon = 0.1$), 10^3 source photons at a monochromatic energy of $E_{\text{phot}} = 6.4 \text{ keV}$, no detector induced noise, no background photons, a constant spacecraft roll of 0.5 mrad per simulator time step, 10 linearly spaced baselines from $D = 5 \text{ cm}$ to $D = 1 \text{ m}$, and all other XRI parameters adopted from Willingale (2004).

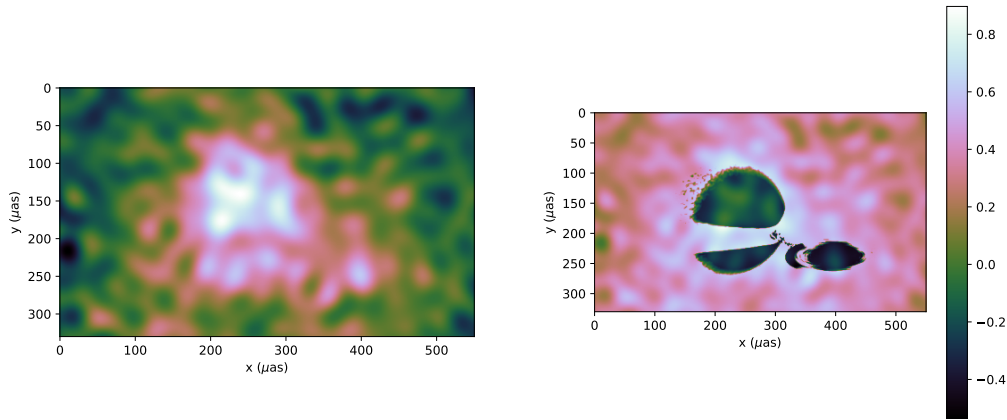


FIG. C.4 – These Figures show the reconstructed image (left) and its residual compared to Figure 2.2 (right), run 1. The image reconstruction used the IFFT reconstruction method ($\epsilon = 0.1$), 10^4 source photons at a monochromatic energy of $E_{\text{phot}} = 6.4 \text{ keV}$, no detector induced noise, no background photons, a constant spacecraft roll of 0.5 mrad per simulator time step, 10 linearly spaced baselines from $D = 5 \text{ cm}$ to $D = 1 \text{ m}$, and all other XRI parameters adopted from Willingale (2004).

Appendix C. Reconstructed images, their respective residuals, and sum of squared residuals values

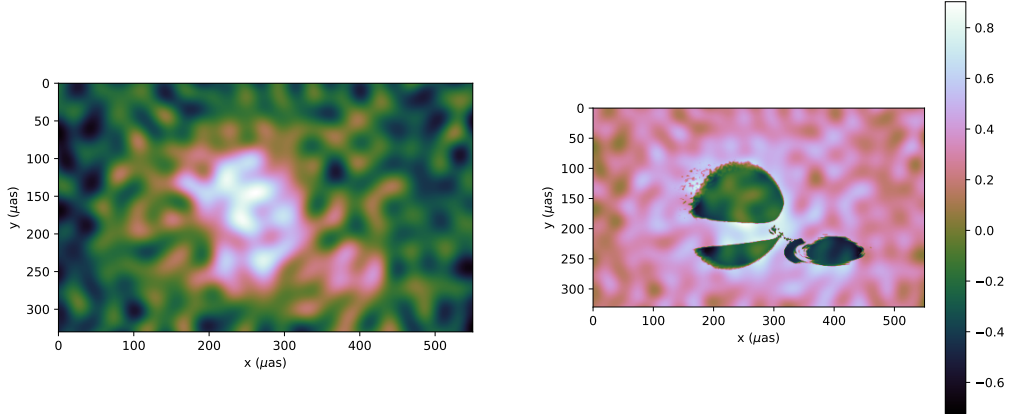


FIG. C.5 – These Figures show the reconstructed image (left) and its residual compared to Figure 2.2 (right), run 2. The image reconstruction used the IFFT reconstruction method ($\epsilon = 0.1$), 10^4 source photons at a monochromatic energy of $E_{\text{phot}} = 6.4 \text{ keV}$, no detector induced noise, no background photons, a constant spacecraft roll of 0.5 mrad per simulator time step, 10 linearly spaced baselines from $D = 5 \text{ cm}$ to $D = 1 \text{ m}$, and all other XRI parameters adopted from [Willingale \(2004\)](#).

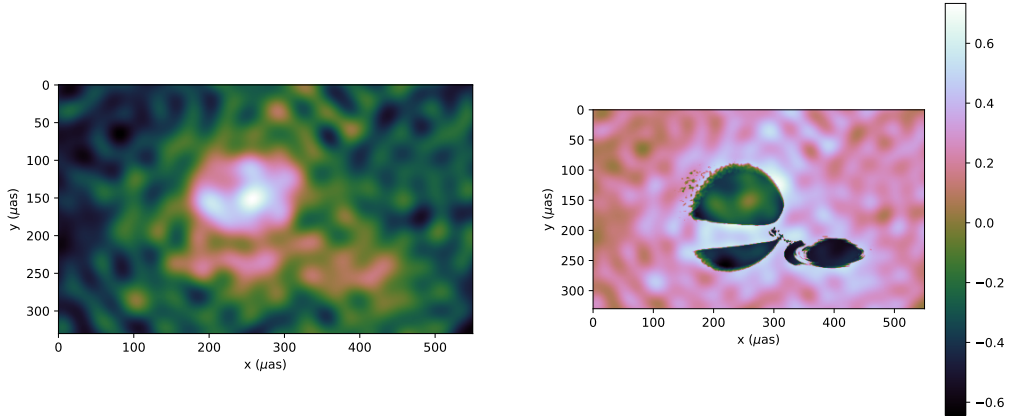


FIG. C.6 – These Figures show the reconstructed image (left) and its residual compared to Figure 2.2 (right), run 3. The image reconstruction used the IFFT reconstruction method ($\epsilon = 0.1$), 10^4 source photons at a monochromatic energy of $E_{\text{phot}} = 6.4 \text{ keV}$, no detector induced noise, no background photons, a constant spacecraft roll of 0.5 mrad per simulator time step, 10 linearly spaced baselines from $D = 5 \text{ cm}$ to $D = 1 \text{ m}$, and all other XRI parameters adopted from [Willingale \(2004\)](#).

Appendix C. Reconstructed images, their respective residuals, and sum of squared residuals values

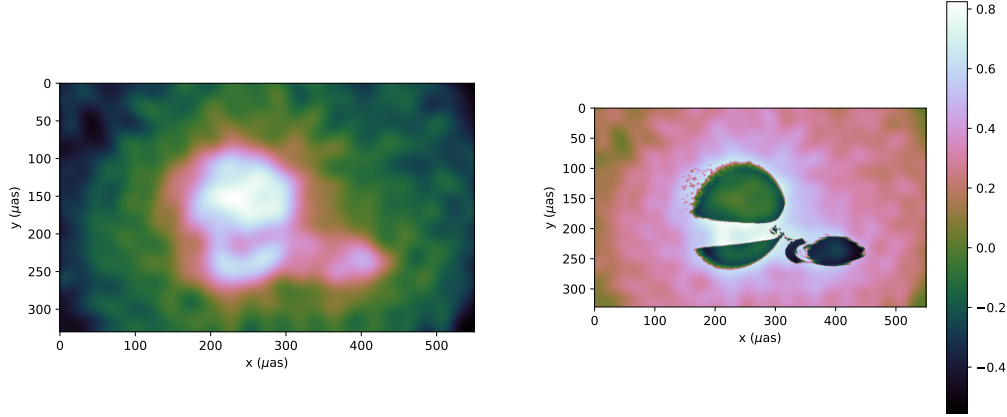


FIG. C.7 – These Figures show the reconstructed image (left) and its residual compared to Figure 2.2 (right), run 1. The image reconstruction used the IFFT reconstruction method ($\epsilon = 0.1$), 10^5 source photons at a monochromatic energy of $E_{\text{phot}} = 6.4 \text{ keV}$, no detector induced noise, no background photons, a constant spacecraft roll of 0.5 mrad per simulator time step, 10 linearly spaced baselines from $D = 5 \text{ cm}$ to $D = 1 \text{ m}$, and all other XRI parameters adopted from Willingale (2004).

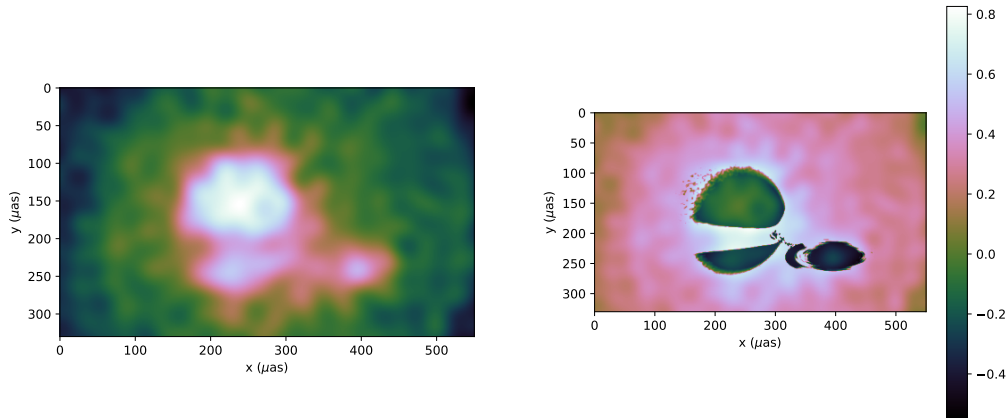


FIG. C.8 – These Figures show the reconstructed image (left) and its residual compared to Figure 2.2 (right), run 2. The image reconstruction used the IFFT reconstruction method ($\epsilon = 0.1$), 10^5 source photons at a monochromatic energy of $E_{\text{phot}} = 6.4 \text{ keV}$, no detector induced noise, no background photons, a constant spacecraft roll of 0.5 mrad per simulator time step, 10 linearly spaced baselines from $D = 5 \text{ cm}$ to $D = 1 \text{ m}$, and all other XRI parameters adopted from Willingale (2004).

Appendix C. Reconstructed images, their respective residuals, and sum of squared residuals values

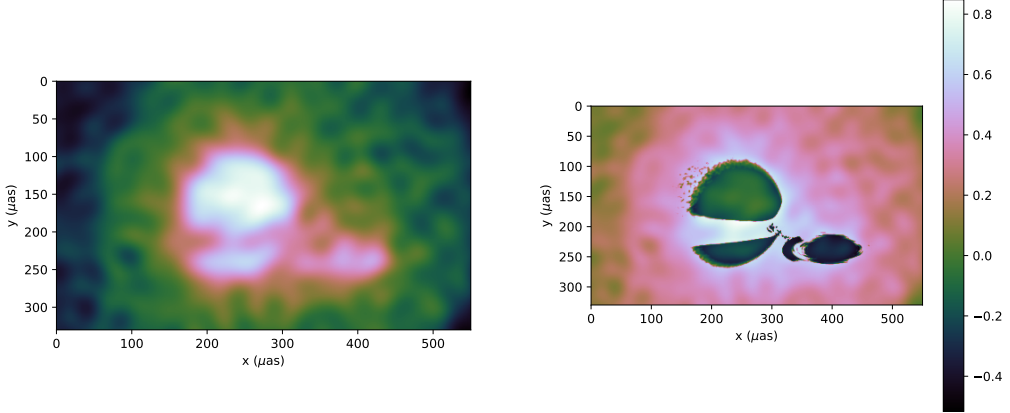


FIG. C.9 – These Figures show the reconstructed image (left) and its residual compared to Figure 2.2 (right), run 3. The image reconstruction used the IFFT reconstruction method ($\epsilon = 0.1$), 10^5 source photons at a monochromatic energy of $E_{\text{phot}} = 6.4 \text{ keV}$, no detector induced noise, no background photons, a constant spacecraft roll of 0.5 mrad per simulator time step, 10 linearly spaced baselines from $D = 5 \text{ cm}$ to $D = 1 \text{ m}$, and all other XRI parameters adopted from [Willingale \(2004\)](#).

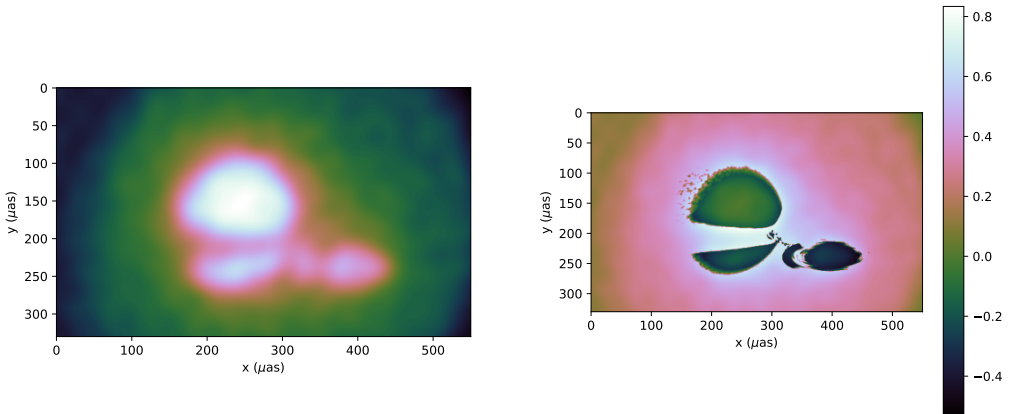


FIG. C.10 – These Figures show the reconstructed image (left) and its residual compared to Figure 2.2 (right), run 1. The image reconstruction used the IFFT reconstruction method ($\epsilon = 0.1$), 10^6 source photons at a monochromatic energy of $E_{\text{phot}} = 6.4 \text{ keV}$, no detector induced noise, no background photons, a constant spacecraft roll of 0.5 mrad per simulator time step, 10 linearly spaced baselines from $D = 5 \text{ cm}$ to $D = 1 \text{ m}$, and all other XRI parameters adopted from [Willingale \(2004\)](#).

Appendix C. Reconstructed images, their respective residuals, and sum of squared residuals values

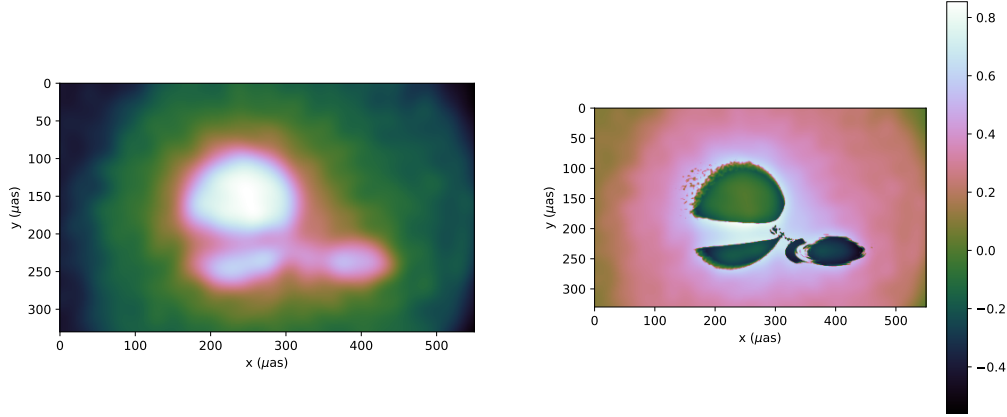


FIG. C.11 – These Figures show the reconstructed image (left) and its residual compared to Figure 2.2 (right), run 2. The image reconstruction used the IFFT reconstruction method ($\epsilon = 0.1$), 10^6 source photons at a monochromatic energy of $E_{\text{phot}} = 6.4 \text{ keV}$, no detector induced noise, no background photons, a constant spacecraft roll of 0.5 mrad per simulator time step, 10 linearly spaced baselines from $D = 5 \text{ cm}$ to $D = 1 \text{ m}$, and all other XRI parameters adopted from [Willingale \(2004\)](#).

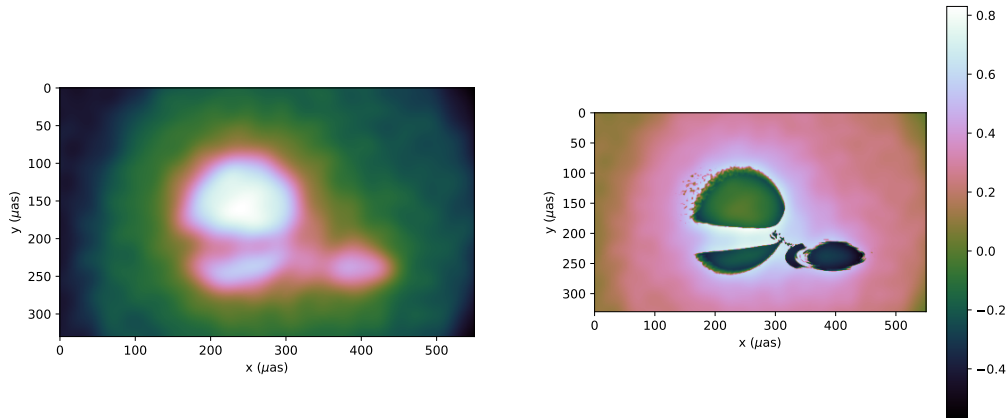


FIG. C.12 – These Figures show the reconstructed image (left) and its residual compared to Figure 2.2 (right), run 3. The image reconstruction used the IFFT reconstruction method ($\epsilon = 0.1$), 10^6 source photons at a monochromatic energy of $E_{\text{phot}} = 6.4 \text{ keV}$, no detector induced noise, no background photons, a constant spacecraft roll of 0.5 mrad per simulator time step, 10 linearly spaced baselines from $D = 5 \text{ cm}$ to $D = 1 \text{ m}$, and all other XRI parameters adopted from [Willingale \(2004\)](#).

Appendix C. Reconstructed images, their respective residuals, and sum of squared residuals values

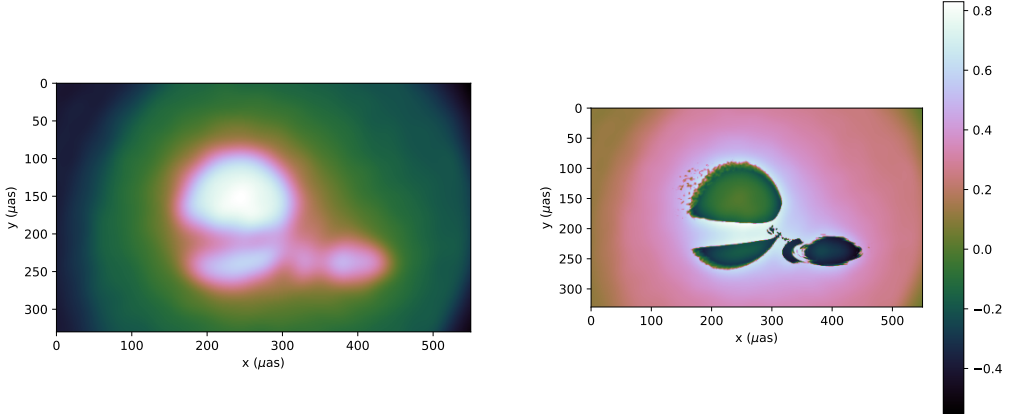


FIG. C.13 – These Figures show the reconstructed image (left) and its residual compared to Figure 2.2 (right), run 1. The image reconstruction used the IFFT reconstruction method ($\epsilon = 0.1$), 10^7 source photons at a monochromatic energy of $E_{\text{phot}} = 6.4 \text{ keV}$, no detector induced noise, no background photons, a constant spacecraft roll of 0.5 mrad per simulator time step, 10 linearly spaced baselines from $D = 5 \text{ cm}$ to $D = 1 \text{ m}$, and all other XRI parameters adopted from Willingale (2004).

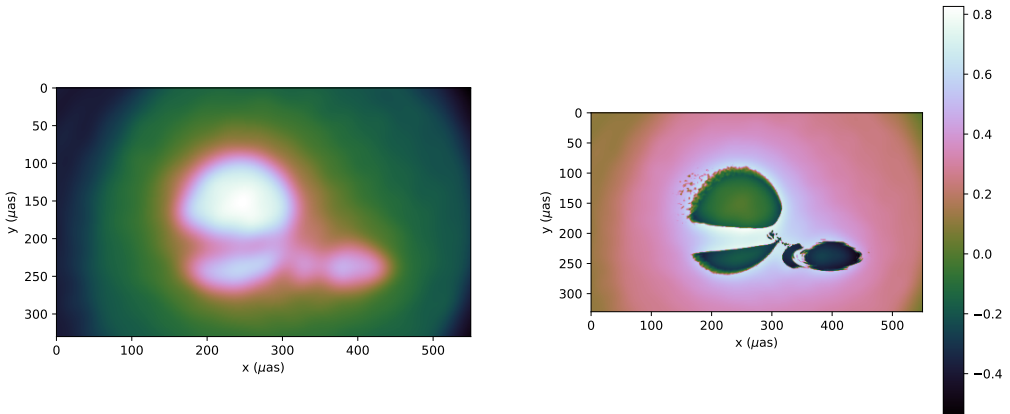


FIG. C.14 – These Figures show the reconstructed image (left) and its residual compared to Figure 2.2 (right), run 2. The image reconstruction used the IFFT reconstruction method ($\epsilon = 0.1$), 10^7 source photons at a monochromatic energy of $E_{\text{phot}} = 6.4 \text{ keV}$, no detector induced noise, no background photons, a constant spacecraft roll of 0.5 mrad per simulator time step, 10 linearly spaced baselines from $D = 5 \text{ cm}$ to $D = 1 \text{ m}$, and all other XRI parameters adopted from Willingale (2004).

Appendix C. Reconstructed images, their respective residuals, and sum of squared residuals values

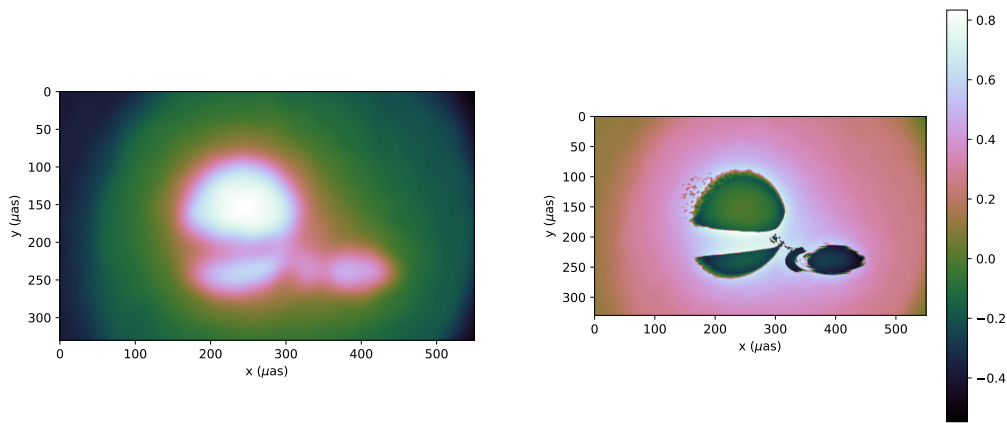


FIG. C.15 – These Figures show the reconstructed image (left) and its residual compared to Figure 2.2 (right), run 3. The image reconstruction used the IFFT reconstruction method ($\epsilon = 0.1$), 10^7 source photons at a monochromatic energy of $E_{\text{phot}} = 6.4 \text{ keV}$, no detector induced noise, no background photons, a constant spacecraft roll of 0.5 mrad per simulator time step, 10 linearly spaced baselines from $D = 5 \text{ cm}$ to $D = 1 \text{ m}$, and all other XRI parameters adopted from [Willingale \(2004\)](#).

Bibliography

- Bachetti, M., Huppenkothen, D., Khan, U., Mishra, H., Stevens, A., Sharma, S., Swinbank, J., Desai, A., Rashid, H., Ribeiro, E. M., Tripathi, M., Sipőcz, B., Vats, D., tappina, Mastroserio, G., omargamal8, Davis, M., Rasquinha, A., Balm, P., Mumford, S., Shukla, D., Campana, R., parkma99, Garg, N., Tandon, A., Hota, A., Anand, A., Nick, Raj, R. & Mishra, S. (2023), ‘Stingraysoftware/stingray: Version 1.1.2’.
- URL:** <https://doi.org/10.5281/zenodo.7970570>
- Blumenthal, G. R. & Tucker, W. H. (1974), Mechanisms for the production of x-rays in a cosmic setting, in ‘X-ray Astronomy’, Springer, pp. 99–153.
- Bolton, C. T. (1972), ‘Identification of cygnus x-1 with hde 226868’, *Nature* **235**, 271–273.
- Bowyer, S., Byram, E. T., Chubb, T. A. & Friedman, H. (1965), ‘Cosmic x-ray sources’, *Science* **147**(3656), 394–398.
- URL:** <https://www.science.org/doi/abs/10.1126/science.147.3656.394>
- Cannon, A. J. & Pickering, E. C. (1918), ‘The Henry Draper catalogue 0h, 1h, 2h, and 3h’, *Annals of Harvard College Observatory* **91**, 1–290.
- Cash, W. (2003), ‘X-ray interferometry’, *Experimental Astronomy* **16**, 91–136.
- Cash, W. C., Gendreau, K. C., Shipley, A. F. & Gallagher, D. J. (2004), Maxim pathfinder: a practical configuration, in ‘Optics for EUV, X-Ray, and Gamma-Ray Astronomy’, Vol. 5168, SPIE, pp. 435–445.
- Cash, W., Shipley, A., Osterman, S. & Joy, M. (2000), ‘Laboratory detection of x-ray fringes with a grazing-incidence interferometer’, *Nature* **407**(6801), 160–162.
- Collaboration, T. E. H. T., Akiyama, K., Alberdi, A., Alef, W., Asada, K., Azulay, R., Bacsko, A.-K., Ball, D., Baloković, M., Barrett, J., Bintley, D., Blackburn, L., Boland, W., Bouman, K. L., Bower, G. C., Bremer, M., Brinkerink, C. D., Brissenden, R., Britzen, S., Broderick, A. E., Broguiere, D., Bronzwaer, T., Byun, D.-Y., Carlstrom, J. E., Chael, A., kwan Chan, C., Chatterjee, S., Chatterjee, K., Chen, M.-T., Chen, Y., Cho, I., Christian, P., Conway, J. E., Cordes, J. M., Crew,

Bibliography

G. B., Cui, Y., Davelaar, J., Laurentis, M. D., Deane, R., Dempsey, J., Desvignes, G., Dexter, J., Doeleman, S. S., Eatough, R. P., Falcke, H., Fish, V. L., Fomalont, E., Fraga-Encinas, R., Freeman, W. T., Friberg, P., Fromm, C. M., Gómez, J. L., Galison, P., Gammie, C. F., García, R., Gentaz, O., Georgiev, B., Goddi, C., Gold, R., Gu, M., Gurwell, M., Hada, K., Hecht, M. H., Hesper, R., Ho, L. C., Ho, P., Honma, M., Huang, C.-W. L., Huang, L., Hughes, D. H., Ikeda, S., Inoue, M., Issaoun, S., James, D. J., Jannuzzi, B. T., Janssen, M., Jeter, B., Jiang, W., Johnson, M. D., Jorstad, S., Jung, T., Karami, M., Karuppusamy, R., Kawashima, T., Keating, G. K., Kettenis, M., Kim, J.-Y., Kim, J., Kim, J., Kino, M., Koay, J. Y., Koch, P. M., Koyama, S., Kramer, M., Kramer, C., Krichbaum, T. P., Kuo, C.-Y., Lauer, T. R., Lee, S.-S., Li, Y.-R., Li, Z., Lindqvist, M., Liu, K., Liuzzo, E., Lo, W.-P., Lobanov, A. P., Loinard, L., Lonsdale, C., Lu, R.-S., MacDonald, N. R., Mao, J., Markoff, S., Marrone, D. P., Marscher, A. P., Martí-Vidal, I., Matsushita, S., Matthews, L. D., Medeiros, L., Menten, K. M., Mizuno, Y., Mizuno, I., Moran, J. M., Moriyama, K., Moscibrodzka, M., Müller, C., Nagai, H., Nagar, N. M., Nakamura, M., Narayan, R., Narayanan, G., Natarajan, I., Neri, R., Ni, C., Noutsos, A., Okino, H., Olivares, H., Ortiz-León, G. N., Oyama, T., Öznel, F., Palumbo, D. C. M., Patel, N., Pen, U.-L., Pesce, D. W., Piétu, V., Plambeck, R., PopStefanija, A., Porth, O., Prather, B., Preciado-López, J. A., Psaltis, D., Pu, H.-Y., Ramakrishnan, V., Rao, R., Rawlings, M. G., Raymond, A. W., Rezzolla, L., Ripperda, B., Roelofs, F., Rogers, A., Ros, E., Rose, M., Roshanineshat, A., Rottmann, H., Roy, A. L., Ruszczyk, C., Ryan, B. R., Rygl, K. L. J., Sánchez, S., Sánchez-Arguelles, D., Sasada, M., Savolainen, T., Schloerb, F. P., Schuster, K.-F., Shao, L., Shen, Z., Small, D., Sohn, B. W., SooHoo, J., Tazaki, F., Tiede, P., Tilanus, R. P. J., Titus, M., Toma, K., Torne, P., Trent, T., Trippe, S., Tsuda, S., van Bemmel, I., van Langevelde, H. J., van Rossum, D. R., Wagner, J., Wardle, J., Weintraub, J., Wex, N., Wharton, R., Wielgus, M., Wong, G. N., Wu, Q., Young, K., Young, A., Younsi, Z., Yuan, F., Yuan, Y.-F., Zensus, J. A., Zhao, G., Zhao, S.-S., Zhu, Z., Algaba, J.-C., Allardi, A., Amestica, R., Anczarski, J., Bach, U., Baganoff, F. K., Beaudoin, C., Benson, B. A., Berthold, R., Blanchard, J. M., Blundell, R., Bustamente, S., Cappallo, R., Castillo-Domínguez, E., Chang, C.-C., Chang, S.-H., Chang, S.-C., Chen, C.-C., Chilson, R., Chuter, T. C., Rosado, R. C., Coulson, I. M., Crawford, T. M., Crowley, J., David, J., Derome, M., Dexter, M., Dornbusch, S., Dudevoir, K. A., Dzib, S. A., Eckart, A., Eckert, C., Erickson, N. R., Everett, W. B., Faber, A., Farah, J. R., Fath, V., Folkers, T. W., Forbes, D. C., Freund, R., Gómez-Ruiz, A. I., Gale, D. M., Gao, F., Geertsema, G., Graham, D. A., Greer, C. H., Grosslein, R., Gueth, F., Haggard, D., Halverson, N. W., Han, C.-C., Han, K.-C., Hao, J., Hasegawa, Y., Henning, J. W., Hernández-Gómez, A., Herrero-Illana, R., Heyminck, S., Hirota, A., Hoge, J., Huang, Y.-D., Impellizzeri, C. M. V., Jiang, H., Kamble, A., Keisler, R., Kimura, K., Kono, Y., Kubo, D., Kuroda, J., Lacasse, R., Laing, R. A., Leitch, E. M., Li, C.-T., Lin, L. C.-C., Liu, C.-T., Liu, K.-Y., Lu, L.-M., Marson, R. G., Martin-Cocher, P. L., Massingill, K. D., Matulonis, C., McColl, M. P., McWhirter, S. R., Messias, H., Meyer-Zhao,

- Z., Michalik, D., Montaña, A., Montgomerie, W., Mora-Klein, M., Muders, D., Nadolski, A., Navarro, S., Neilsen, J., Nguyen, C. H., Nishioka, H., Norton, T., Nowak, M. A., Nystrom, G., Ogawa, H., Oshiro, P., Oyama, T., Parsons, H., Paine, S. N., Peñalver, J., Phillips, N. M., Poirier, M., Pradel, N., Primiani, R. A., Raffin, P. A., Rahlin, A. S., Reiland, G., Risacher, C., Ruiz, I., Sáez-Madaín, A. F., Sassella, R., Schellart, P., Shaw, P., Silva, K. M., Shiokawa, H., Smith, D. R., Snow, W., Souccar, K., Sousa, D., Sridharan, T. K., Srinivasan, R., Stahm, W., Stark, A. A., Story, K., Timmer, S. T., Vertatschitsch, L., Walther, C., Wei, T.-S., Whitehorn, N., Whitney, A. R., Woody, D. P., Wouterloot, J. G. A., Wright, M., Yamaguchi, P., Yu, C.-Y., Zeballos, M., Zhang, S. & Ziurys, L. (2019), 'First m87 event horizon telescope results. i. the shadow of the supermassive black hole', *The Astrophysical Journal Letters* **875**(1), L1.
URL: <https://dx.doi.org/10.3847/2041-8213/ab0ec7>
- Czesla, S., Huber, K., Wolter, U., Schröter, S. & Schmitt, J. (2009), 'How stellar activity affects the size estimates of extrasolar planets', *Astronomy & Astrophysics* **505**(3), 1277–1282.
- Donati, J. F., Cristofari, P. I., Finocci, B., Klein, B., Moutou, C., Gaidos, E., Cadieux, C., Artigau, E., Correia, A. C. M., Boué, G., Cook, N. J., Carmona, A., Lehmann, L. T., Bouvier, J., Martioli, E., Morin, J., Fouqué, P., Delfosse, X., Doyon, R., Hébrard, G., Alencar, S. H. P., Laskar, J., Arnold, L., Petit, P., Kóspál, Á., Vidotto, A., Folsom, C. P. & collaboration, t. S. L. S. (2023), 'The magnetic field and multiple planets of the young dwarf AU Mic', *Monthly Notices of the Royal Astronomical Society* **525**(1), 455–475.
- Donati, J., Moutou, C., Malo, L., Baruteau, C., Yu, L., Hébrard, E., Hussain, G., Alencar, S., Ménard, F., Bouvier, J. et al. (2016), 'A hot jupiter orbiting a 2-million-year-old solar-mass t tauri star', *Nature* **534**(7609), 662–666.
- Drake, J. J. & Stelzer, B. (2022), *Stellar Coronae*, Springer Nature Singapore, Singapore, pp. 1–72.
URL: https://doi.org/10.1007/978-981-16-4544-0_78-1
- Garde, A. (2023), Interaction diffraction patterns of multiple slat-gap pairs. Placeholder title, in prep.
- Gendreau, K., Arzoumanian, Z., Cash, W., Fabian, A., Gorenstein, P., George, I. et al. (2009), 'The science enabled by ultrahigh angular resolution x-ray and gamma-ray imaging of black holes', *astro2010: The Astronomy and Astrophysics Decadal Survey* **2010**, 87.
- Gendreau, K. C., Cash, W. C., Gorenstein, P., Windt, D. L., Kaaret, P. & Reynolds, C. (2004), Maxim: the black hole imager, in 'UV and Gamma-Ray Space Telescope Systems', Vol. 5488, SPIE, pp. 394–402.

Bibliography

- Gendreau, K. C., Leitner, J., Markley, L., Cash, W. C. & Shipley, A. F. (2003), Requirements and options for a stable inertial frame for a 100-micro-arcsecond imaging telescope, in ‘Interferometry in Space’, Vol. 4852, SPIE, pp. 685–694.
- Giacobbo, N. & Mapelli, M. (2018), ‘The progenitors of compact-object binaries: impact of metallicity, common envelope and natal kicks’, *Monthly Notices of the Royal Astronomical Society* **480**(2), 2011–2030.
URL: <https://doi.org/10.1093/mnras/sty1999>
- Gou, L., McClintock, J. E., Reid, M. J., Orosz, J. A., Steiner, J. F., Narayan, R., Xiang, J., Remillard, R. A., Arnaud, K. A. & Davis, S. W. (2011), ‘The extreme spin of the black hole in cygnus x-1’, *The Astrophysical Journal* **742**(2), 85.
- Grinberg, V., Hell, N., El Mellah, I., Neilsen, J., Sander, A., Leutenegger, M., Fürst, F., Huenemoerder, D., Kretschmar, P., Kühnel, M. et al. (2017), ‘The clumpy absorber in the high-mass x-ray binary vela x-1’, *Astronomy & Astrophysics* **608**, A143.
- Güdel, M. (2004), ‘X-ray astronomy of stellar coronae’, *The Astronomy and Astrophysics Review* **12**, 71–237.
- Hecht, E. (2017), *Optics*, Global 5th edn, Pearson Education Limited, Edinburgh Gate, Harlow, CM20 2JE, England. Authorized adaptation from the U.S. 5th edition, ISBN: 9780133977226.
- Heinemans, P. (2020), X-ray interferometry: Revealing the high energy universe with ultra-high spatial resolution, Bachelor’s thesis, Anton Pannekoek Institute & University of Amsterdam.
- Huan, X. & Marzouk, Y. (2014), ‘Gradient-based stochastic optimization methods in bayesian experimental design’, *International Journal for Uncertainty Quantification* **4**(6), 479–510.
URL: <http://dx.doi.org/10.1615/Int.J.UncertaintyQuantification.2014006730>
- Klein, B., Donati, J.-F., Moutou, C., Delfosse, X., Bonfils, X., Martioli, E., Fouqué, P., Cloutier, R., Artigau, É., Doyon, R., Hébrard, G., Morin, J., Rameau, J., Plavchan, P. & Gaidos, E. (2021), ‘Investigating the young AU Mic system with SPIRou: large-scale stellar magnetic field and close-in planet mass’, *Monthly Notices of the Royal Astronomical Society* **502**(1), 188–205.
- Kudritzki, R.-P. & Puls, J. (2000), ‘Winds from hot stars’, *Annual Review of Astronomy and Astrophysics* **38**(1), 613–666.
URL: <https://doi.org/10.1146/annurev.astro.38.1.613>
- Lagier, R. (2021), *Ariane 6 User’s Manual Issue 2 Revision 0*, ArianeSpace, Bd de l’Europe, 91006 Évry-Courcouronnes, France. Available at https://www.arianespace.com/wp-content/uploads/2021/03/Mua-6_Issue-2_Revision-0_March-2021.pdf.

- Manhart, M. & Meidinger, N. (2018), Wfi system budgets, Technical Report WFI-MPE-TRE-0020, SRON, Niels Bohrweg 4, 2333 CA Leiden. Internal report, restricted acces.
- Martínez-Núñez, S., Kretschmar, P., Bozzo, E., Osokinova, L. M., Puls, J., Sidoli, L., Sundqvist, J. O., Blay, P., Falanga, M., Fürst, F. et al. (2017), ‘Towards a unified view of inhomogeneous stellar winds in isolated supergiant stars and supergiant high mass x-ray binaries’, *Space Science Reviews* **212**, 59–150.
- Martioli, E., Hébrard, G., Correia, A. C. M., Laskar, J. & Lecavelier des Etangs, A. (2021), ‘New constraints on the planetary system around the young active star AU Mic. Two transiting warm Neptunes near mean-motion resonance’, *Astronomy & Astrophysics* **649**, A177.
- Meidinger, N., Ott, S. & Plattner, M. (2018), Wfi design definition file, Technical Report WFI-MPE-DDF-0010, SRON, Niels Bohrweg 4, 2333 CA Leiden. Internal report, restricted acces.
- Miller-Jones, J. C. A., Bahramian, A., Orosz, J. A., Mandel, I., Gou, L., Maccarone, T. J., Neijssel, C. J., Zhao, X., Ziolkowski, J., Reid, M. J., Uttley, P., Zheng, X., Byun, D.-Y., Dodson, R., Grinberg, V., Jung, T., Kim, J.-S., Marcote, B., Markoff, S., Rioja, M. J., Rushton, A. P., Russell, D. M., Sivakoff, G. R., Tetarenko, A. J., Tudose, V. & Wilms, J. (2021), ‘Cygnus x-1 contains a 21–solar mass black hole—implications for massive star winds’, *Science* **371**(6533), 1046–1049.
URL: <https://www.science.org/doi/abs/10.1126/science.abb3363>
- Mori, K., Tsunemi, H., Miyata, E., Baluta, C. J., Burrows, D. N., Garmire, G. P. & Chartas, G. (2001), Improvement of the chandra acis spatial resolution by selecting the split pixel events, in ‘New Century of X-ray Astronomy’, Vol. 251, p. 576.
- Muñoz-Darias, T., Casares, J., Sánchez, D. M., Fender, R., Padilla, M. A., Linares, M., Ponti, G., Charles, P., Mooley, K. & Rodriguez, J. (2016), ‘Regulation of black-hole accretion by a disk wind during a violent outburst of v404 cygni’, *Nature* **534**(7605), 75–78.
- Oda, M. (1977), ‘Cygx-1/a candidate of the black hole’, *Space Science Reviews* **20**(6), 757–813.
- Oda, M., Gorenstein, P., Gursky, H., Kellogg, E., Schreier, E., Tananbaum, H. & Giacconi, R. (1971), ‘X-Ray Pulsations from Cygnus X-1 Observed from UHURU’, *Astrophysical Journal* **166**, L1.
- Orosz, J. A., McClintock, J. E., Aufdenberg, J. P., Remillard, R. A., Reid, M. J., Narayan, R. & Gou, L. (2011), ‘The mass of the black hole in cygnus x-1’, *The Astrophysical Journal* **742**(2), 84.

Bibliography

- Plavchan, P., Barclay, T., Gagné, J., Gao, P., Cale, B., Matzko, W., Dragomir, D., Quinn, S., Feliz, D., Stassun, K., Crossfield, I. J. M., Berardo, D. A., Latham, D. W., Tieu, B., Anglada-Escudé, G., Ricker, G., Vanderspek, R., Seager, S., Winn, J. N., Jenkins, J. M., Rinehart, S., Krishnamurthy, A., Dynes, S., Doty, J., Adams, F., Afanasev, D. A., Beichman, C., Bottom, M., Bowler, B. P., Brinkworth, C., Brown, C. J., Cancino, A., Ciardi, D. R., Clampin, M., Clark, J. T., Collins, K., Davison, C., Foreman-Mackey, D., Furlan, E., Gaidos, E. J., Geneser, C., Giddens, F., Gilbert, E., Hall, R., Hellier, C., Henry, T., Horner, J., Howard, A. W., Huang, C., Huber, J., Kane, S. R., Kenworthy, M., Kielkopf, J., Kipping, D., Klenke, C., Kruse, E., Latouf, N., Lowrance, P., Mennesson, B., Mengel, M., Mills, S. M., Morton, T., Narita, N., Newton, E., Nishimoto, A., Okumura, J., Palle, E., Pepper, J., Quintana, E. V., Roberge, A., Roccatagliata, V., Schlieder, J. E., Tanner, A., Teske, J., Tinney, C. G., Vanderburg, A., von Braun, K., Walp, B., Wang, J., Wang, S. X., Weigand, D., White, R., Wittenmyer, R. A., Wright, D. J., Youngblood, A., Zhang, H. & Zilberman, P. (2020), ‘A planet within the debris disk around the pre-main-sequence star AU Microscopii’, *Nature* **582**(7813), 497–500.
- Ponti, G., Fender, R. P., Begelman, M. C., Dunn, R. J. H., Neilsen, J. & Coriat, M. (2012), ‘Ubiquitous equatorial accretion disc winds in black hole soft states’, *Monthly Notices of the Royal Astronomical Society: Letters* **422**(1), L11–L15.
URL: <https://doi.org/10.1111/j.1745-3933.2012.01224.x>
- Ponti, G., George, E., Scaringi, S., Zhang, S., Jin, C., Dexter, J., Terrier, R., Clavel, M., Degenaar, N., Eisenhauer, F. et al. (2017), ‘A powerful flare from sgr a* confirms the synchrotron nature of the x-ray emission’, *Monthly Notices of the Royal Astronomical Society* **468**(2), 2447–2468.
- Poppenhaeger, K., Schmitt, J. & Wolk, S. (2013), ‘Transit observations of the hot jupiter hd 189733b at x-ray wavelengths’, *The Astrophysical Journal* **773**(1), 62.
- Reid, M. J., McClintock, J. E., Narayan, R., Gou, L., Remillard, R. A. & Orosz, J. A. (2011), ‘The trigonometric parallax of cygnus x-1’, *The Astrophysical Journal* **742**(2), 83.
URL: <https://dx.doi.org/10.1088/0004-637X/742/2/83>
- Riley, T. E., Choudhury, D., Salmi, T., Vinciguerra, S., Kini, Y., Dorsman, B., Watts, A. L., Huppenkothen, D. & Guillot, S. (2023), ‘X-PSI: A Python package for neutron star X-ray pulse simulation and inference’, *Journal of Open Source Software* **8**(82), 4977.
URL: <https://doi.org/10.21105/joss.04977>
- Shields, G. A., McKee, C. F., Lin, D. N. C. & Begelman, M. C. (1986), ‘Compton-heated Winds and Coronae above Accretion Disks. III. Instability and Oscillations’, *Astrophysical Journal* **306**, 90.
- Sriramanathan, S. (2024), Astrovaria project. Placeholder title, in prep.

- Stirling, A., Spencer, R., de La Force, C., Garrett, M., Fender, R. & Ogle, R. (2001), ‘A relativistic jet from Cygnus X-1 in the low/hard X-ray state’, *Monthly Notices of the Royal Astronomical Society* **327**(4), 1273–1278.
URL: <https://doi.org/10.1046/j.1365-8711.2001.04821.x>
- Svendsen, S., Massahi, S., Ferreira, D. D. M., Christensen, F., Jafari, A., Henriksen, P., Collon, M., Landgraf, B., Girou, D., Krumrey, M. et al. (2019), Performance and time stability of ir/sic x-ray mirror coatings for athena, in ‘Optics for EUV, X-Ray, and Gamma-Ray Astronomy IX’, Vol. 11119, SPIE, pp. 131–140.
- Uttley, P. (2024), A fourier approach to x-ray fringe finding. In prep.
- Uttley, P., den Hartog, R., Bambi, C., Barret, D., Bianchi, S., Bursa, M., Cappi, M., Casella, P., Cash, W., Costantini, E. et al. (2020), An x-ray interferometry concept for the esa voyage 2050 programme, in ‘Space Telescopes and Instrumentation 2020: Ultraviolet to Gamma Ray’, Vol. 11444, SPIE, pp. 146–162.
- Uttley, P., Hartog, R. d., Bambi, C., Barret, D., Bianchi, S., Bursa, M., Cappi, M., Casella, P., Cash, W., Costantini, E. et al. (2021), ‘The high energy universe at ultra-high resolution: the power and promise of x-ray interferometry’, *Experimental Astronomy* **51**(3), 1081–1107.
- van Dokkum, P. G., Bloom, J. & Tewes, M. (2012), ‘L.A.Cosmic: Laplacian Cosmic Ray Identification’, Astrophysics Source Code Library, record ascl:1207.005.
- Van Eyken, J. C., Ciardi, D. R., Von Braun, K., Kane, S. R., Plavchan, P., Bender, C. F., Brown, T. M., Crepp, J. R., Fulton, B. J., Howard, A. W. et al. (2012), ‘The ptf orion project: a possible planet transiting a t-tauri star’, *The Astrophysical Journal* **755**(1), 42.
- van Hese, E. (2023), Simulation of a proposed x-ray interferometry satellite, Master’s thesis, Anton Pannekoek Institute & University of Amsterdam & Vrije Universiteit Amsterdam.
- Watanabe, S., Sako, M., Ishida, M., Ishisaki, Y., Kahn, S. M., Kohmura, T., Nagase, F., Paerels, F. & Takahashi, T. (2006), ‘X-ray spectral study of the photoionized stellar wind in vela x-1’, *The Astrophysical Journal* **651**(1), 421.
- Webster, B. L. & Murdin, P. (1972), ‘Cygnus x-1—a spectroscopic binary with a heavy companion?’, *Nature* **235**, 37–38.
- Willingale, R. (2004), A practical system for x-ray interferometry, in ‘UV and Gamma-Ray Space Telescope Systems’, Vol. 5488, SPIE, pp. 581–592.
- Wittrock, J. M., Plavchan, P. P., Cale, B. L., Barclay, T., Ludwig, M. R., Schwarz, R. P., Mékarnia, D., Triaud, A. H. M. J., Abe, L., Suarez, O., Guillot, T., Conti, D. M., Collins, K. A., Waite, I. A., Kielkopf, J. F., Collins, K. I., Dreizler, S., El

Bibliography

- Mufti, M., Feliz, D. L., Gaidos, E., Geneser, C. S., Horne, K. D., Kane, S. R., Lowrance, P. J., Martioli, E., Radford, D. J., Reefe, M. A., Roccatagliata, V., Shporer, A., Stassun, K. G., Stockdale, C., Tan, T.-G., Tanner, A. M. & Vega, L. D. (2023), ‘Validating AU Microscopii d with Transit Timing Variations’, *The Astronomical Journal* **166**(6), 232.
- Wolter, H. (1952a), ‘Spiegelsysteme streifenden einfalls als abbildende optiken für röntgenstrahlen’, *Annalen der Physik* **445**(1-2), 94–114.
- Wolter, H. (1952b), ‘Verallgemeinerte Schwarzschildsche Spiegelsysteme streifender Reflexion als Optiken für Röntgenstrahlen’, *Annalen der Physik* **445**(4), 286–295.